Automatic quantum circuit encoding of a given arbitrary quantum state

Tomonori Shirakawa, ^{1,2} Hiroshi Ueda, ^{3,1,4} and Seiji Yunoki, ^{1,2,5,6}

¹Computational Materials Science Research Team, RIKEN Center for Computational Science (R-CCS), Kobe, Hyogo 650-0047, Japan
²Quantum Computational Science Research Team, RIKEN Center for Quantum Computing (RQC), Wako, Saitama 351-0198, Japan
³Center for Quantum Information and Quantum Biology, Osaka University, Toyonaka, Osaka 560-8531, Japan
⁴JST, PRESTO, Kawaguchi, 332-0012, Japan

⁵Computational Quantum Matter Research Team, RIKEN Center for Emergent Matter Science (CEMS), Wako, Saitama 351-0198, Japan

⁶Computational Condensed Matter Physics Laboratory, RIKEN Cluster for Pioneering Research (CPR), Saitama 351-0198, Japan



(Received 30 December 2021; accepted 17 September 2024; published 3 October 2024)

We introduce an quantum-classical hybrid algorithm, named automatic quantum circuit encoding (AQCE), that is designed to encode an arbitrary quantum state $|\Psi\rangle$ onto an optimal quantum circuit \hat{C} composed of a finite set of single- and two-qubit quantum gates. The algorithm employs an objective function based on the absolute value of fidelity, $F = \langle 0|\hat{C}^{\dagger}|\Psi\rangle$, which is iteratively maximized to construct an optimal quantum circuit \hat{C} with controlled accuracy. Here, $|0\rangle$ denotes a trivial product state in the computational basis of a quantum computer. The core of this algorithm lies in the sequential determination of an optimal set of two-qubit unitary operators, identified one by one through the singular value decomposition of the fidelity tensor. Once an optimal set of operators is determined, including the location of qubits on which each operator acts, elementary quantum gates are assigned algebraically to these two-qubit unitary operators. Importantly, these procedures are deterministic without assuming any quantum circuit ansatz and therefore eliminate the need for parameter optimization of parametrized quantum gates. Through noiseless numerical simulations, we demonstrate the effectiveness of the AQCE algorithm in encoding ground states of quantum many-body systems, including the spin-1/2 antiferromagnetic Heisenberg model and the spin-1/2 XY model. We also compare these results with quantum circuit encoding employing predefined circuit structures such as Trotter-like and MERA-like circuit ansatze. Furthermore, our algorithm extends to classical data, for instance, classical images represented as quantum states using amplitude encoding. The adaptability enables us to adjust the quantum resource requirement, i.e., the number of qubits, by partitioning classical data into multiple distinct segments. This feature holds potential for near-term applications in quantum machine learning, such as a state preparation of classical data for an input quantum state to be processed. Finally, using a real quantum device provided by IBM Quantum, we experimentally validate that a quantum circuit generated by the AQCE algorithm can indeed reasonably represent the original quantum state.

DOI: 10.1103/PhysRevResearch.6.043008

I. INTRODUCTION

It has been of crucial importance to find useful applications of quantum computers specially since the realization of real programable quantum devices. Considering that currently available quantum devices are prone to noise and decoherence, it is highly desirable to find applications that can work effectively with a less number of quantum gates and qubits. Under these conditions, one of the promising and appealing approaches is based on variational quantum algorithms [1] because it can be applied to a wide range of applications

Published by the American Physical Society under the terms of the Creative Commons Attribution 4.0 International license. Further distribution of this work must maintain attribution to the author(s) and the published article's title, journal citation, and DOI.

including quantum chemistry [2–9] and quantum machine learning [10–19].

In variational quantum algorithms, a quantum circuit is composed of parametrized quantum gates and these parameters are optimized classically on a classical computer to minimize or maximize a cost function by using standard optimization techniques such as a natural gradient descent method [20–22] and a sequential optimization technique [23]. In this context, there is an issue, known as barren plateau (BP) phenomena, where the partial derivatives of the cost function vanish exponentially with increasing the number of qubits and quantum gates [24-27]. The basic tool used to discuss the BP phenomena is the unitary t-design [28] related to the representability of a quantum circuit via the Haar measure [29,30]. The theory of the BP phenomenon [24] claims that a quantum circuit which shows unitary 2-design exhibits the BP phenomena. Generally, one tends to increase the number of quantum gates to represent a quantum state that one intends to prepare in the first place. However, such a quantum circuit with enhanced capability of representation can easily fall into the class of unitary operators belonging to the unitary 2-design [31,32], thus suggesting the emergence of the BP phenomena [33].

Several routes have been discussed to alleviate and even avoid the BP phenomena. A simplest way is to select a cost function appropriately because the BP phenomena is cost function dependent [25]. The importance of properly setting the initial variational parameters has also been pointed out [34,35]. Another route to address the BP issue is to construct an appropriate quantum circuit. For instance, it has been reported that a quantum circuit with a structure like the multi-scale entanglement renormalization group ansatz (MERA) [36-38], known also as quantum convolutional neural network [39], can avoid the BP phenomena [40]. However, the tensor network structure of MERA is originally constructed to capture the quantum entanglement of a particular quantum state, e.g., in a one-dimensional critical system, and therefore it is not obvious at all and is probably not appropriate that the MERA-type quantum circuit can be applied to general problems. An alternative approach in this regard is a method such as adapted variational quantum eigensolver (ADAPT-VQE) [41–45], where an appropriate quantum circuit is automatically generated by selecting quantum gates sequentially among a predetermined set of quantum gates accordingly to a problem to be solved.

Following a similar strategy of the ADAPT-VQE, here in this paper, we propose a method that constructs an appropriate quantum circuit automatically, named automatic quantum circuit encoding (AQCE). The AQCE algorithm proposed here is to construct a quantum circuit \hat{C} that approximates a given quantum state $|\Psi\rangle$ such that $|\Psi\rangle\approx\hat{\mathcal{C}}|0\rangle$ with controlled accuracy. Here, \hat{C} is composed of a standard set of quantum gates acting on up to two qubits and $|0\rangle$ is a trivial product state in the computational basis. The algorithm is not based on a parametrized circuit ansatz but determines sequentially optimal two-qubit unitary operators, including an optimal location of qubits on which each unitary operator acts, by maximizing the fidelity with a technique inspired by the optimization algorithm in the tensor-network method [38]. A standard set of quantum gates is assigned algebraically to these optimally determined unitary operators. Therefore, the AQCE algorithm does not requires any derivatives of a cost function.

With noiseless numerical simulations, we demonstrate the AQCE algorithm to encode a ground state of quantum many-body systems including the spin-1/2 isotropic antiferromagnetic Heisenberg model and the spin-1/2 XY model. We also compare the results with the quantum circuit encoding of the same quantum state onto a quantum circuit in a given circuit structure (i.e., a quantum circuit ansatz) such as the Trotter-like [46–48] and MERA-like circuit structures. Furthermore, we apply this algorithm to encode classical data that is represented as a quantum state via the amplitude encoding [15], demonstrating a potential near-term application for a quantum state preparation of input data in quantum machine learning. In addition, we employ a real quantum device provided by IBM Quantum [49] to demonstrate

experimentally that a quantum circuit generated by the AQCE algorithm can indeed represent the original quantum state reasonably.

The rest of this paper is organized as follows. The AQCE algorithm is first introduced in Sec. II. The performance of this algorithm is then demonstrated by numerical simulations in Sec. III. The method is first applied to encode the ground states of the spin-1/2 Heisenberg models in Sec. III A, and the results are compared with those for the quantum circuit encoding of the same quantum states onto quantum circuits with fixed circuit structures in Sec. III B. The results are also compared with those obtained for parametrized quantum circuit encoding optimized by a gradient-based method in Sec. III C. The application of the AQCE algorithm to classical data such as a classical image represented by a quantum state via the amplitude encoding is also discussed in Sec. IIID. Moreover, the AOCE algorithm is partially demonstrated experimentally with a real quantum device in Sec. IV. Finally, the paper is concluded with a brief summary in Sec. V. The details of the gate assignment of unitary operators acting on a single qubit and on two qubits are described in Appendices A and B. Additional information for the experimental demonstration is provided in Appendix C.

II. QUANTUM CIRCUIT ENCODING ALGORITHM

We first introduce the fidelity as an objective function for quantum circuit encoding in Sec. II A. We then describe how to determine a unitary matrix of a quantum gate operation by maximizing the objective function in Sec. IIB. Based on these techniques, we introduce a prototype of the algorithm for the quantum circuit encoding in Sec. II C. We also explain how to evaluate the fidelity tensor elements on a quantum computer in Sec. IID. Although the encoding algorithm can be applied in any cases, it might meet some difficulty when the fidelity tensor is essentially zero due to a particular symmetry reason. We discuss this issue and introduce an alternative approach to overcome this problem in Sec. IIE. This approach can be used for the initialization of the quantum circuit encoding. Combining with these methods in Secs. IIC and IIE, we finally introduce an algorithm, i.e., the AQCE algorithm, to construct a quantum circuit automatically in Sec. IIF.

A. Objective for quantum circuit encoding

We consider a quantum state defined on L qubits that are enumerated as $\mathbb{L}=\{1,2,\cdots,i,\cdots,L\}$. Let $\hat{X}_i,\,\hat{Y}_i$, and \hat{Z}_i denote the $x,\,y,\,$ and z components of the Pauli operators, respectively, acting on qubit i. We also introduce the notation \hat{I}_i for representing the identity operator on qubit i. Let $|\sigma_i\rangle_i=|0\rangle_i$ and $|1\rangle_i$ denote the eigenstates of the Pauli operator \hat{Z}_i at qubit $i,\,$ i.e., $\hat{Z}_i|0\rangle_i=|0\rangle_i$ and $\hat{Z}_i|1\rangle=-|1\rangle_i.$ The Hilbert space \mathbb{H}_L on the L-qubit system \mathbb{L} is spanned by the basis $\{|\sigma_1\sigma_2\cdots\sigma_L\rangle\}$, where $|\sigma_1\sigma_2\cdots\sigma_L\rangle=\otimes_{i=1}^L|\sigma_i\rangle_i.$ We can label the state $|\sigma_1\sigma_2\cdots\sigma_L\rangle$ by introducing the integer number

$$n = \sum_{i=1}^{L} 2^{i-1} \sigma_i \tag{1}$$

as $\{|n\rangle = |\sigma_1\sigma_2\cdots\sigma_L\rangle\}_{n=0}^{2^L-1}$ in the Hilbert space $\mathbb{H}_L = \operatorname{span}\{|\sigma_1\sigma_2\cdots\sigma_L\rangle\}$.

Let $|\Psi\rangle$ be an arbitrary quantum state defined on $\mathbb L$ and let us assume that $|\Psi\rangle$ is normalized. In addition, we can assume that $|\Psi\rangle$ is given generally by a linear combination of many different quantum circuit states, i.e.,

$$|\Psi\rangle = \sum_{\gamma=1}^{\Gamma} \chi_{\gamma} |\psi^{(\gamma)}\rangle, \tag{2}$$

with

$$|\psi^{(\gamma)}\rangle = \hat{\psi}^{(\gamma)}|0\rangle,\tag{3}$$

where χ_{γ} and $\hat{\psi}^{(\gamma)}$ with $\gamma=1,2,\cdots,\Gamma$ are complex-valued coefficients and quantum circuits, respectively. Although $\langle \psi^{(\gamma)}|\psi^{(\gamma)}\rangle=1$, i.e., $\hat{\psi}^{(\gamma)}$ being unitary, here we do not assume that the states $|\psi^{(\gamma)}\rangle$ with different values of γ are mutually orthogonal. Note that Eq. (2) may include the simplest and most extreme case where the circuits $\hat{\psi}_{\gamma}$ are composed simply of products of Pauli-X operators

$$\hat{\mathcal{P}}_{\{\sigma_i\}_{i=1}^L} \equiv \prod_{i=1}^L \hat{X}_i^{\sigma_i},\tag{4}$$

i.e., $\hat{\mathcal{P}}_{\{\sigma_i\}_{i=1}^L}|0\rangle = |\sigma_1\sigma_2\cdots\sigma_L\rangle$, as in the case of a quantum state representing a classical image via the amplitude encoding discussed in Sec. III D. The objective here is to represent $|\Psi\rangle$ by a quantum circuit $\hat{\mathcal{C}}|0\rangle$ that is *a priori* unknown. The algorithm proposed here constructs a quantum circuit $\hat{\mathcal{C}}$ that approximately represents $|\Psi\rangle \approx \hat{\mathcal{C}}|0\rangle$ with controlled accuracy. We should note that this can be considered as a special case in the variational quantum state eigensolver for a density operator reported in Ref. [50], although the optimization method introduced here is different, as it will be described below.

For this purpose, we consider as an objective function to be maximized the absolute value of the overlap F between $|\Psi\rangle$ and $\hat{\mathcal{C}}|0\rangle$, i.e.,

$$F = \langle 0|\hat{\mathcal{C}}^{\dagger}|\Psi\rangle. \tag{5}$$

Assuming that the quantum circuit \hat{C} is composed of a product of unitary operators \hat{U}_m , i.e.,

$$\hat{\mathcal{C}}^{\dagger} = \prod_{m=1}^{M} \hat{\mathcal{U}}_{m}^{\dagger} = \hat{\mathcal{U}}_{1}^{\dagger} \hat{\mathcal{U}}_{2}^{\dagger} \cdots \hat{\mathcal{U}}_{M}^{\dagger}, \tag{6}$$

F can be expressed as

$$F_m = \langle \Phi_{m-1} | \hat{\mathcal{U}}_m^{\dagger} | \Psi_{m+1} \rangle, \tag{7}$$

where we have introduced the subscript m explicitly for the reason clarified below and the quantum states $|\Psi_m\rangle$ and $\langle\Phi_m|$ defined, respectively, as

$$|\Psi_{m}\rangle = \prod_{k=m}^{M} \hat{\mathcal{U}}_{k}^{\dagger} |\Psi\rangle = \hat{\mathcal{U}}_{m}^{\dagger} \hat{\mathcal{U}}_{m+1}^{\dagger} \cdots \hat{\mathcal{U}}_{M}^{\dagger} |\Psi\rangle \tag{8}$$

and

$$\langle \Phi_m | = \langle 0 | \prod_{k=1}^m \hat{\mathcal{U}}_k^{\dagger} = \langle 0 | \hat{\mathcal{U}}_1^{\dagger} \hat{\mathcal{U}}_2^{\dagger} \cdots \hat{\mathcal{U}}_m^{\dagger}, \tag{9}$$

with $|\Psi_{M+1}\rangle = |\Psi\rangle$ and $|\Phi_0\rangle = |0\rangle$.

B. Determination of unitary operators

To appropriately determine each unitary operator $\hat{\mathcal{U}}_m$ composing the quantum circuit $\hat{\mathcal{C}}$, here we propose a method inspired by a tensor-network algorithm [38] by introducing a fidelity tensor operator.

Let $\mathbb{I}_m = \{i_1, i_2, \cdots, i_K\}$ with $1 \leqslant i_1 < i_2 < \cdots < i_K \leqslant L$ be a subsystem in the total L-qubit system \mathbb{L} and assume that an unitary operator $\hat{\mathcal{U}}_m$ is defined on the subsystem \mathbb{I}_m . By labeling the basis states $\{|n\rangle = |\sigma_{i_1}\sigma_{i_2}\cdots\sigma_{i_K}\rangle\}_{n=0}^{2^K-1}$ on the subsystem \mathbb{I}_m , i.e., $n = \sum_{k=1}^K 2^{k-1}\sigma_{i_k}$, the unitary operator $\hat{\mathcal{U}}_m$ can be represented generally as

$$\hat{\mathcal{U}}_{m} = \sum_{n=0}^{2^{K}-1} \sum_{n'=0}^{2^{K}-1} |n\rangle [U_{m}]_{nn'} \langle n'|, \tag{10}$$

where U_m is a $2^K \times 2^K$ unitary matrix and $[A]_{nn'}$ denotes a matrix element in the *n*th row and the *n'*th column of matrix A.

We shall now introduce the following fidelity tensor operator $\hat{\mathcal{F}}_m$:

$$\hat{\mathcal{F}}_m = \operatorname{Tr}_{\bar{\mathbb{I}}_m}[|\Psi_{m+1}\rangle\langle\Phi_{m-1}|],\tag{11}$$

where $\bar{\mathbb{I}}_m$ is the complement of the subsystem \mathbb{I}_m in \mathbb{L} and $\mathrm{Tr}_{\mathbb{A}}\hat{\mathcal{O}}$ indicates the trace of operator $\hat{\mathcal{O}}$ over the Hilbert space spanned by the basis states for subsystem $\mathbb{A} = \{i_1, i_2, \cdots, i_A\} \subset \mathbb{L}$, i.e.,

$$\operatorname{Tr}_{\mathbb{A}}[\hat{\mathcal{O}}] = \sum_{\sigma_{i_1}=0}^{1} \sum_{\sigma_{i_2}=0}^{1} \cdots \sum_{\sigma_{i_A}=0}^{1} \langle \sigma_{i_1} \sigma_{i_2} \cdots \sigma_{i_A} | \hat{\mathcal{O}} | \sigma_{i_1} \sigma_{i_2} \cdots \sigma_{i_A} \rangle,$$
(12)

with $|\sigma_{i_1}\cdots\sigma_{i_A}\rangle = |\sigma_{i_1}\rangle_{i_1}|\sigma_{i_2}\rangle_{i_2}\cdots|\sigma_{i_A}\rangle_{i_A}$ and $1\leqslant i_1\leqslant i_2\leqslant\cdots\leqslant i_A\leqslant L$. Since $\hat{\mathcal{F}}_m$ is an operator defined on the Hilbert space spanned by the basis states for the subsystem \mathbb{I}_m , one can represent the operator $\hat{\mathcal{F}}_m$ in the matrix form as

$$\hat{\mathcal{F}}_{m} = \sum_{n=0}^{2^{K}-1} \sum_{n'=0}^{2^{K}-1} |n\rangle [\mathbf{F}_{m}]_{nn'} \langle n'|.$$
 (13)

We can now readily find that

$$\operatorname{Tr}_{\mathbb{I}_m}[\hat{\mathcal{F}}_m\hat{\mathcal{U}}_m^{\dagger}] = \langle \Phi_{m-1} | \hat{\mathcal{U}}_m^{\dagger} | \Psi_{m+1} \rangle = F_m. \tag{14}$$

We also find that

$$\operatorname{Tr}_{\mathbb{I}_m}[\hat{\mathcal{F}}_m\hat{\mathcal{U}}_m^{\dagger}] = \operatorname{tr}[\boldsymbol{F}_m\boldsymbol{U}_m^{\dagger}],\tag{15}$$

where trA indicates the trace of matrix A. Note that F_m is a $2^K \times 2^K$ matrix and is neither Hermitian nor unitary in general.

Let us now perform the singular-value decomposition (SVD) for F_m as

$$\boldsymbol{F}_{m} \stackrel{\text{SVD}}{=} \boldsymbol{X} \boldsymbol{D} \boldsymbol{Y}, \tag{16}$$

where X and Y are $2^K \times 2^K$ unitary matrices, and D is a non-negative real diagonal matrix with its diagonal elements being the singular values d_n $(n = 0, 1, 2, \dots, 2^K - 1)$ of matrix F_m . Note that the m dependence of these matrices X, Y, and D is

implicitly assumed. We then find that

$$F_m = \operatorname{tr}[\boldsymbol{X}\boldsymbol{D}\boldsymbol{Y}\boldsymbol{U}_m^{\dagger}] = \operatorname{tr}[\boldsymbol{D}\boldsymbol{Z}] = \sum_{n=0}^{2^K - 1} d_n[\boldsymbol{Z}]_{nn}, \quad (17)$$

where $\mathbf{Z} = YU_m^{\dagger}X$ is a unitary matrix. The absolute value of F_m thus satisfies that

$$|F_m| = \left| \sum_{n=0}^{2^K - 1} d_n [\mathbf{Z}]_{nn} \right| \leqslant \sum_{n=0}^{2^K - 1} d_n |[\mathbf{Z}]_{nn}|.$$
 (18)

The equality in Eq. (18) holds if and only if $\arg[[\mathbf{Z}]_{nn}]$ is the same for all n, where $\arg[c]$ denotes the phase of complex number c. Noticing also that $\sum_{n'} |[\mathbf{Z}]_{nn'}|^2 = \sum_{n'} |[\mathbf{Z}]_{n'n}|^2 = 1$ because \mathbf{Z} is unitary, the absolute value of F_m is thus maximized by choosing $[\mathbf{Z}]_{nn'} = \delta_{nn'}$ [51], i.e., $\mathbf{Z} = \mathbf{I}$, where \mathbf{I} is the identity matrix. Hence, the unitary matrix \mathbf{U}_m that maximizes the absolute value of F_m is obtained as

$$\boldsymbol{U}_{m} = \boldsymbol{X}\boldsymbol{Y},\tag{19}$$

and therefore we can determine the optimal unitary operator $\hat{\mathcal{U}}_m$. Summarizing these results, the following corollary is obtained:

Corollary 1. Let $|\Psi\rangle$ be an given quantum state and $|\Phi\rangle$ be a quantum circuit state given by $\hat{\mathcal{U}}_M\hat{\mathcal{U}}_{M-1}\cdots\hat{\mathcal{U}}_1|0\rangle$. Fixing unitary operators $\{\hat{\mathcal{U}}_i\}_{i=1}^M$ other than the *m*th unitary operator $\hat{\mathcal{U}}_m$ acting on subsystem \mathbb{I}_m , the optimal $\hat{\mathcal{U}}_m$ that maximizes the absolute value of the fidelity $F = \langle \Psi | \Phi \rangle$ is given by

$$\arg\max_{\hat{\mathcal{U}}_m}[|F|] = \sum_{n,n'} |n\rangle_{\mathbb{I}_m}[XY]_{nn'\mathbb{I}_m} \langle n'|, \qquad (20)$$

where X and Y are the unitary matrices obtained by the singular-value decomposition of \mathbf{F}_m , the matrix representation of the fidelity tensor operator $\hat{\mathcal{F}}_m$ given in Eq. (11), and $|n\rangle_{\mathbb{I}_m}$ denotes the basis states on subsystem \mathbb{I}_m .

Three remarks are in order. First, as already stated above, a similar idea is used in the optimization of tensor network states [38]. Second, although the fidelity tensor $\hat{\mathcal{F}}_m$ can be defined for a subsystem containing many qubits, we focus mostly on the two-qubit case in this paper. This is simply because the assignment of elementary quantum gates for an optimal unitary operator determined in Eq. (19) can be made rather simply, as described in the next section. Third, the fidelity F_m and the fidelity tensor operator $\hat{\mathcal{F}}_m$ can be more explicitly expressed for the case when the state $|\Psi\rangle$ is given by a linear combination of several quantum states as in Eq. (2), i.e.,

$$F_m = \sum_{\gamma=1}^{\Gamma} \chi_{\gamma} f_m^{(\gamma)} \tag{21}$$

and

$$\hat{\mathcal{F}}_m = \sum_{\gamma=1}^{\Gamma} \chi_{\gamma} \hat{f}_m^{(\gamma)},\tag{22}$$

where

$$f_m^{(\gamma)} = \text{Tr}_{\mathbb{I}_m} \left[\hat{f}_m^{(\gamma)} \hat{\mathcal{U}}_m^{\dagger} \right] \tag{23}$$

and

$$\hat{f}_{m}^{(\gamma)} = \operatorname{Tr}_{\bar{\mathbb{I}}_{m}} \left[\left| \psi_{m+1}^{(\gamma)} \right\rangle \langle \Phi_{m-1} | \right], \tag{24}$$

with

$$\left|\psi_{m}^{(\gamma)}\right\rangle = \hat{\mathcal{U}}_{m}^{\dagger} \hat{\mathcal{U}}_{m+1}^{\dagger} \cdots \hat{\mathcal{U}}_{M}^{\dagger} |\psi^{(\gamma)}\rangle. \tag{25}$$

The optimal unitary operator $\hat{\mathcal{U}}_m$ that maximizes the absolute value of F_m is still determined by Eqs. (17)–(19).

Once we obtain the matrix representation U_m for the unitary operator by using the above technique, we have to assign a standard set of elementary quantum gates to this operator $\hat{\mathcal{U}}_m$. It is well known that any unitary operator can be compiled as a product of two-qubit quantum gates by using the method that proves the universality of quantum computation [52]. However, this method of decomposing a unitary operator acting on K qubits generates an exponentially large number of elementary single- and two-qubit quantum gates with respect to K. Therefore, it is not practical for our purpose. In contrast, focusing on a unitary operator acting on two qubits, there exists an optimal form decomposing it into elementary quantum gates [53], which can be determined from its matrix representation U_m (See Appendix A). Therefore, in what follows, we consider how to construct a circuit composed of the product of two-qubit quantum gates.

C. Quantum circuit encoding algorithm

Using the procedures described above, we can now introduce an algorithm to construct a quantum circuit $\hat{\mathcal{C}}$ that approximately represents a given quantum state $|\Psi\rangle$. Without loss of generality, let us assume that $\hat{\mathcal{C}}^\dagger = \prod_{m=1}^M \hat{\mathcal{U}}_m^\dagger$ is given. For example, we set $\hat{\mathcal{U}}_m = \hat{I}$ for all m as the initial condition, where \hat{I} is the identity operator of the subspace defining $\hat{\mathcal{U}}_m$. In the algorithm, we sequentially replaces $\hat{\mathcal{U}}_m$ to a new $\hat{\mathcal{U}}_m'$ that maximizes the absolute value of the fidelity

$$F_m = \langle \Phi_{m-1} | (\hat{\mathcal{U}}'_m)^{\dagger} | \Psi_{m+1} \rangle, \tag{26}$$

where $\langle \Phi_{m-1} |$ and $| \Psi_{m+1} \rangle$ are given, respectively, by

$$\langle \Phi_{m-1} | = \langle 0 | \prod_{m'=1}^{m-1} (\hat{\mathcal{U}}'_{m'})^{\dagger} = \langle 0 | (\hat{\mathcal{U}}'_1)^{\dagger} (\hat{\mathcal{U}}'_2)^{\dagger} \cdots (\hat{\mathcal{U}}'_{m-1})^{\dagger}$$
 (27)

and

$$|\Psi_{m+1}\rangle = \prod_{m'=m+1}^{M} (\hat{\mathcal{U}}_{m'})^{\dagger} |\Psi\rangle = (\hat{\mathcal{U}}_{m+1})^{\dagger} (\hat{\mathcal{U}}_{m+2})^{\dagger} \cdots (\hat{\mathcal{U}}_{M})^{\dagger} |\Psi\rangle,$$
(28)

with $|\Phi_0\rangle = |0\rangle$ and $|\Psi_{M+1}\rangle = |\Psi\rangle$. Furthermore, we assume that the *m*th two-qubit unitary operator $\hat{\mathcal{U}}_m$ acting on $\mathbb{I}_m = \{i_m, j_m\}$ is replaced with an unitary operator $\hat{\mathcal{U}}'_m$ acting on $\mathbb{I}_k = \{i_k, j_k\}$ that is properly selected among a set of bonds $\mathbb{B} = \{\mathbb{I}_1, \mathbb{I}_2, \dots, \mathbb{I}_B\}$. Although here we assume the case of two-qubit unitary operators, the generalization to *K*-qubit unitary operators with K > 2 is straightforward.

A prototype of the algorithm is then given in Algorithm 1 and is also schematically shown in Fig. 1(a). Here, the symbol ":=" in the algorithm denotes that the variable on the left

ALGORITHM 1. Forward update.

```
Input Target state |\Psi\rangle, quantum circuit \hat{C} = \hat{U}_M \hat{U}_{M-1} \cdots \hat{U}_1,
and a set of bonds \mathbb{B} = {\mathbb{I}_1, \mathbb{I}_2, \cdots, \mathbb{I}_B}
     Output Updated quantum circuit \hat{C}' = \hat{U}'_M \hat{U}'_{M-1} \cdots \hat{U}'_1
 1: function FORWARD|\Psi\rangle, \mathcal{C}, \mathbb{B}
2: Set \hat{\mathcal{C}}' := \hat{I}, |\Psi'\rangle := \prod_{m'=2}^{M} (\hat{\mathcal{U}}_{m'})^{\dagger} |\Psi\rangle, and \langle \Phi'| := \langle 0|.
           for m = 1, 2, \dots, M do
 3:
                 Evaluate matrix F_m^{(k)} of the fidelity tensor operator
      \hat{\mathcal{F}}_m^{(k)} = \mathrm{Tr}_{\bar{\mathbb{I}}_k}[|\Psi'\rangle\langle\Phi'|] \text{ for all } \mathbb{I}_k \in \mathbb{B}.
                 Perform SVD F_m^{(k)} = X_k D_k Y_k and calculate
 5:
      S_k =
                 Find k = k^* that maximizes S_k among k = 1, 2, \dots, B.
                 Set U := X_{k*}Y_{k*} and assign the quantum gates for the
      new mth unitary operator \hat{\mathcal{U}}_m', represented by the matrix U,
      acting on \mathbb{I}_m := \mathbb{I}_{k^*} = \{i_{k^*}, j_{k^*}\}.
                 Set \hat{C}' := \hat{\mathcal{U}}'_{...}\hat{C}'.
 8:
 9:
                 if m \neq M then
                     Set |\Psi'\rangle := \hat{\mathcal{U}}_{m+1}|\Psi'\rangle, \langle \Phi'| := \langle \Phi'|(\hat{\mathcal{U}}_m')^{\dagger}.
10:
               end if
11:
12:
        end for
        return \hat{\mathcal{C}}'
13:
14: end Function
```

side is newly replaced with the variable on the right side. Algorithm 1 describes the sequential update of the unitary operators from m = 1 to m = M [also see Fig. 1(a)] and thus we refer to this update as forward update.

However, it is apparent that the order of update can be reversed, from m=M to m=1, as shown in Fig. 1(b). The algorithm for this is given in Algorithm 2 and is referred to as backward update. Note that the procedure at line 4 in both Algorithm 1 and Algorithm 2 is most time consuming and can be treated on a quantum computer (see Sec. II D), while the other procedures are performed on a classical computer. Since the evaluation of $F_m^{(k)}$ for different bonds \mathbb{I}_k is independent, one can trivially parallelize this part. The underlying assumption in Algorithms 1 and 2 is that the sequential update in order form m=1 to m=M and vice versa is computationally efficient when it is performed on a classical computer. The computational complexity is further discussed later in Sec. II F.

Finally, we shall refer to a single set of consecutive updates, forward update followed by backward update, as a sweep. As summarized in Algorithm 3, we aim to optimize the entire quantum circuit by repeating the sweeps.

D. Implementation on a quantum computer

The most demanding part computationally in the quantum circuit encoding algorithm is to evaluate the fidelity tensor operator $\hat{\mathcal{F}}_m$ in Eq. (11). As explained here, this part can be evaluated directly using a quantum computer when the quantum state $|\Psi\rangle$ is given by a linear combination of several quantum circuits as in Eq. (2), which includes the extreme case where $|\Psi\rangle$ is given by a linear combination of direct product states in the computational basis.

Although this procedure can be extended to the case for any number of qubits in principle, here we consider a subsystem

(a) Forward update

Input:
$$\hat{\mathcal{C}} := -\hat{\mathcal{U}}_M - \hat{\mathcal{U}}_{M-1} - \cdots - \hat{\mathcal{U}}_2 - \hat{\mathcal{U}}_1 - , |\Psi\rangle, \mathbb{B}$$

$$\hat{\mathcal{F}}_{1} \quad \boxed{\langle 0|} \quad \stackrel{\downarrow}{\longleftarrow} \quad \stackrel{\downarrow}{\mathcal{U}_{2}^{\dagger}} \quad \cdots \quad \stackrel{\downarrow}{\mathcal{U}_{M-1}^{\dagger}} \quad \stackrel{\downarrow}{\mathcal{U}_{M}^{\dagger}} \quad |\Psi\rangle \quad \Rightarrow \quad \hat{\mathcal{U}}_{1}^{\dagger} \quad \Rightarrow \quad \hat{\mathcal{U}}_{1}^{\dagger}} \\
\hat{\mathcal{F}}_{2} \quad \boxed{\langle 0|} \quad \stackrel{\downarrow}{\mathcal{U}_{1}^{\dagger}} \quad \stackrel{\downarrow}{\longleftarrow} \quad \stackrel{\downarrow}{\longleftarrow} \quad \stackrel{\downarrow}{\mathcal{U}_{M-1}^{\dagger}} \quad \stackrel{\downarrow}{\mathcal{U}_{M}^{\dagger}} \quad |\Psi\rangle \quad \Rightarrow \quad \hat{\mathcal{U}}_{2}^{\dagger} \quad \Rightarrow \quad \hat{\mathcal{U}}_{2}^{\dagger}} \\
\vdots \\
\hat{\mathcal{F}}_{M-1} \quad \boxed{\langle 0|} \quad \stackrel{\downarrow}{\mathcal{U}_{1}^{\dagger}} \quad \stackrel{\downarrow}{\mathcal{U}_{2}^{\dagger}} \quad \cdots \quad \stackrel{\downarrow}{\longleftarrow} \quad \stackrel{\downarrow}{\mathcal{U}_{M-1}^{\dagger}} \quad \stackrel{\downarrow}{\Psi}\rangle \quad \Rightarrow \quad \hat{\mathcal{U}}_{M-1}^{\dagger} \quad \Rightarrow \quad \hat{\mathcal{U}}_{M-1}^{\dagger}} \\
\hat{\mathcal{F}}_{M} \quad \boxed{\langle 0|} \quad \stackrel{\downarrow}{\mathcal{U}_{1}^{\dagger}} \quad \stackrel{\downarrow}{\mathcal{U}_{2}^{\dagger}} \quad \cdots \quad \stackrel{\downarrow}{\mathcal{U}_{M-1}^{\dagger}} \quad \stackrel{\downarrow}{\Psi}\rangle \quad \Rightarrow \quad \hat{\mathcal{U}}_{M}^{\dagger} \quad \Rightarrow \quad$$

(b) Backward update

$$\left(\text{Input: } \hat{\mathcal{C}} := - \left(\hat{\mathcal{U}}_{M} - \hat{\mathcal{U}}_{M-1} - \cdots - \left(\hat{\mathcal{U}}_{2} - \hat{\mathcal{U}}_{1} - , \right. \right. |\Psi\rangle, \ \mathbb{B} \right)$$

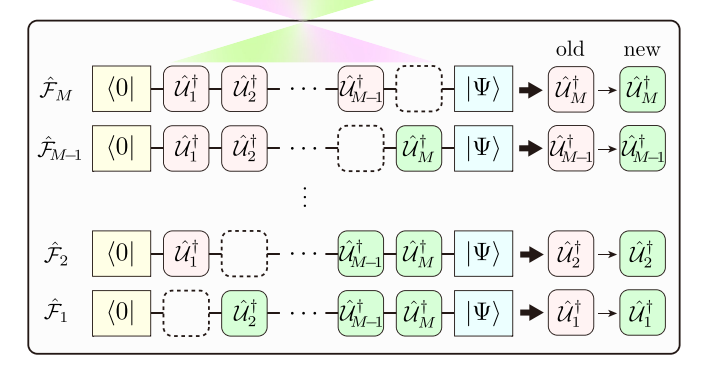


FIG. 1. (a) Forward and (b) backward updates that optimize sequentially unitary operators $\hat{\mathcal{U}}_m$ for $m=1,2,\cdots,M$. Light-blue boxes with rounded corners indicate the input unitary operators, while light-red and light-green boxes with rounded corners indicate the updated unitary operators by forward and backward updates, respectively. Light-yellow and light-blue square boxes indicate the initial product state $|0\rangle$ and the target state $|\Psi\rangle$, respectively. Evaluating the fidelity tensor operators $\hat{\mathcal{F}}_m^{(k)} = \mathrm{Tr}_{\mathbb{I}_k} [\hat{\mathcal{U}}_{m+1}^\dagger \cdots \hat{\mathcal{U}}_{M}^\dagger |\Psi\rangle\langle 0|\hat{\mathcal{U}}_1^\dagger \cdots \hat{\mathcal{U}}_{m-1}^\dagger$ for all $\mathbb{I}_k \in \mathbb{B} = \{\mathbb{I}_1, \mathbb{I}_2, \cdots, \mathbb{I}_B\}$ and performing the SVD for the corresponding matrices $F_m^{(k)}$, we select the optimal mth unitary operator $\hat{\mathcal{U}}_m$ acting on bond \mathbb{I}_k that maximizes the absolute value of the fidelity (see Algorithms 1 and 2).

composed of two qubits, i.e., $\mathbb{I}_m = \{i, j\}$, on which an unitary operator $\hat{\mathcal{U}}_m$ acts. Let us introduce the following notation:

$$\hat{\mathcal{P}}_{i}^{\alpha} = \begin{cases} \hat{I}_{i} & (\alpha = 0), \\ \hat{X}_{i} & (\alpha = 1), \\ \hat{Y}_{i} & (\alpha = 2), \\ \hat{Z}_{i} & (\alpha = 3), \end{cases}$$
 (29)

for the identity and Pauli operators acting on qubit *i*. Then, the fidelity tensor operator $\hat{\mathcal{F}}_m$ in the two-qubit subsystem $\mathbb{I}_m = \{i, j\}$ can be expressed generally as

$$\hat{\mathcal{F}}_m = \sum_{\alpha=0}^3 \sum_{\alpha'=0}^3 \tilde{f}_{\alpha,\alpha'} \hat{\mathcal{P}}_i^{\alpha} \hat{\mathcal{P}}_j^{\alpha'}, \tag{30}$$

ALGORITHM 2. Backward update.

```
Input Target state |\Psi\rangle, quantum circuit \hat{C} = \hat{U}_M \hat{U}_{M-1} \cdots \hat{U}_1,
and a set of bonds \mathbb{B} = {\mathbb{I}_1, \mathbb{I}_2, \cdots, \mathbb{I}_B}
        Output Updated quantum circuit \hat{C}' = \hat{\mathcal{U}}'_{M} \hat{\mathcal{U}}'_{M-1} \cdots \hat{\mathcal{U}}'_{1}
        function BACKWARD|\Psi\rangle, \mathcal{C}, \mathbb{B}
  1:
              Set \hat{\mathcal{C}}' := \hat{I}, |\Psi'\rangle := |\Psi\rangle, and \langle \Phi'| := \langle 0| \prod_{m'=1}^{M-1} \hat{\mathcal{U}}_{m'}^{\dagger}.
 2:
               for m = M, M - 1, \dots, 1 do
 3:
                     Evaluate matrix F_m^{(k)} of the fidelity tensor operator
               = \operatorname{Tr}_{\bar{\mathbb{I}}_k}[|\Psi'\rangle\langle\Phi'|] for all \mathbb{I}_k \in \mathbb{B}.
                     Perform SVD F_m^{(k)} = X_k D_k Y_k and calculate
 5:
       S_k = \sum_{n=0}^3 [\boldsymbol{D}_k]_{nn}.
                     Find k = k^* that maximizes S_k among
 7:
                     Set U := X_{k^*}Y_{k^*} and assign the quantum gates for the
       new mth unitary operator \hat{\mathcal{U}}_m', represented by the matrix U,
       acting on \mathbb{I}_m := \mathbb{I}_{k^*} = \{i_{k^*}, j_{k^*}\}.
 8:
                     Set \hat{C}' := \hat{C}' \hat{\mathcal{U}}'_m.
 9:
                     if m \neq 1 then
                        Set |\Psi'\rangle := (\hat{\mathcal{U}}_m')^{\dagger} |\Psi'\rangle, \langle \Phi'| := \langle \Phi'|\hat{\mathcal{U}}_{m-1}.
10:
11:
                   end if
               end for
12:
13:
              return \hat{\mathcal{C}}'
14: end Function
```

where $\tilde{f}_{\alpha,\alpha'}$ are complex numbers. This is simply because the operator $|n\rangle\langle n'|$ in Eq. (13) for all n,n'=0,1,2,3 can be expanded with a polynomial of the Pauli and identity operators. We thus find that

$$\operatorname{Tr}_{\mathbb{I}_m} \left[\hat{\mathcal{F}}_m \hat{\mathcal{P}}_i^{\alpha} \hat{\mathcal{P}}_i^{\alpha'} \right] = 2^2 \tilde{f}_{\alpha,\alpha'}, \tag{31}$$

because

$$\operatorname{Tr}_{\mathbb{I}_m} \left[\hat{\mathcal{P}}_i^{\beta} \hat{\mathcal{P}}_j^{\beta'} \hat{\mathcal{P}}_i^{\alpha} \hat{\mathcal{P}}_j^{\alpha'} \right] = 2^2 \delta_{\alpha,\beta} \delta_{\alpha',\beta'}. \tag{32}$$

Meanwhile, by using the definition of the fidelity tensor operator $\hat{\mathcal{F}}_m$ in Eq. (11), we find that

$$\operatorname{Tr}_{\mathbb{I}_m} \left[\hat{\mathcal{F}}_m \hat{\mathcal{P}}_i^{\alpha} \hat{\mathcal{P}}_j^{\alpha'} \right] = \langle \Phi_{m-1} | \hat{\mathcal{P}}_i^{\alpha} \hat{\mathcal{P}}_j^{\alpha'} | \Psi_{m+1} \rangle. \tag{33}$$

Therefore, $\tilde{f}_{\alpha,\alpha'}$ can be determined by estimating the overlap between $\hat{\mathcal{P}}_{i}^{\alpha}\hat{\mathcal{P}}_{j}^{\alpha'}|\Psi_{m+1}\rangle$ and $|\Phi_{m-1}\rangle$ for all $\alpha,\alpha'=0,1,2,3$. This overlap can be evaluated using a Hadamard test like circuit shown in Fig. 2(a), provided that a quantum circuit $\hat{\Psi}$ generating the quantum state $|\Psi\rangle = \hat{\Psi}|0\rangle$ is already known. However, this is generally not the case but rather the main task

ALGORITHM 3. Sweep.

```
Input Target state |\Psi\rangle, quantum circuit
\hat{\mathcal{C}} = \hat{\mathcal{U}}_M \hat{\mathcal{U}}_{M-1} \cdots \hat{\mathcal{U}}_1, a set of bonds \mathbb{B}, and integer N
        Output Optimal quantum circuit \hat{C}'
  1: function SWEEP|\Psi\rangle, \hat{C}, \mathbb{B}, N
              for n = 1, 2, \dots, N do
  2:
                     \hat{\mathcal{C}} := \text{FORWARD}(|\Psi\rangle, \hat{\mathcal{C}}, \mathbb{B}).
  3:
                     \hat{\mathcal{C}} := \text{BACKWARD}(|\Psi\rangle, \hat{\mathcal{C}}, \mathbb{B}).
  4:
  5:
              end for
              Set \hat{C}' := \hat{C}.
  6:
              return \hat{\mathcal{C}}'
  7:
  8: end Function
```

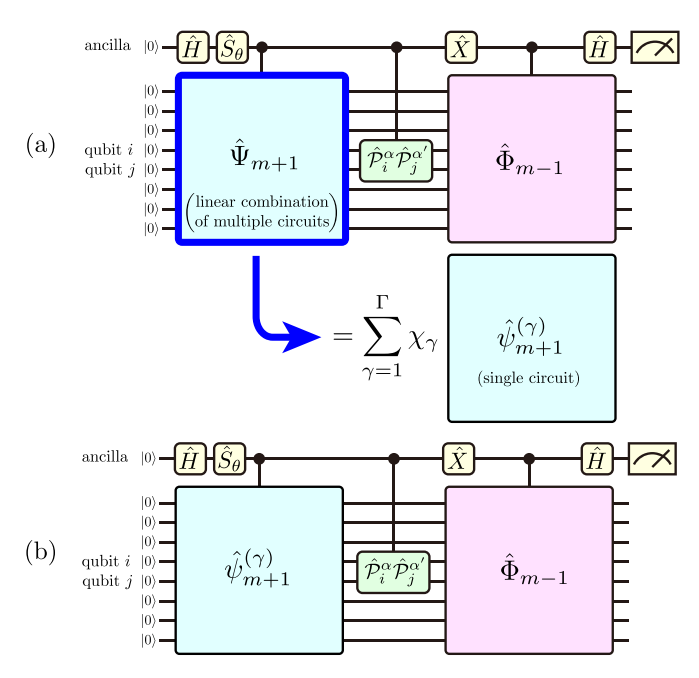


FIG. 2. (a) A quantum circuit to evaluate Eq. (33). \hat{H} and \hat{X} are Hadamard and Pauli-X gates, respectively. \hat{S}_{θ} is a phase shift gate given by $\hat{S}_{\theta}|0\rangle = |0\rangle$ and $\hat{S}_{\theta}|1\rangle = e^{-i\theta}|1\rangle$. The quantum circuits $\hat{\Psi}_{m+1}$ and $\hat{\Phi}_{m-1}$ are defined as $|\Psi_{m+1}\rangle = \prod_{k=m+1}^M \hat{\mathcal{U}}_k^{\dagger} |\Psi\rangle = \hat{\Psi}_{m+1}|0\rangle$ and $|\Phi_{m-1}\rangle = \prod_{k=m-1}^1 \hat{\mathcal{U}}_k |0\rangle = \hat{\Phi}_{m-1}|0\rangle$, respectively. In our protocol, we assume that $|\Psi\rangle$ is given by a linear combination of quantum circuit states $|\psi^{(y)}\rangle$, including the extreme case where it is given by a linear combination of direct product states in the computational basis. Therefore, as indicated in the figure, $\hat{\Psi}_{m+1}$ is given by a linear combination of different quantum circuits, i.e., $\hat{\Psi}_{m+1} = \sum_{\gamma=1}^{\Gamma} \chi_{\gamma} \hat{\psi}_{m+1}^{(\gamma)}$, where $\hat{\psi}_{m+1}^{(\gamma)} = \prod_{k=m+1}^{M} \hat{\mathcal{U}}_k^{\dagger} \hat{\psi}_{m+1}^{(\gamma)}$ and $|\psi^{(\gamma)}\rangle = \hat{\psi}^{(\gamma)}|0\rangle$. Hence, $f_{\alpha,\alpha'}^{(\gamma)} = \langle \Phi_{m-1}|\hat{\mathcal{P}}_{n}^{\alpha}\hat{\mathcal{P}}_{j}^{\alpha'}|\psi_{m+1}^{(\gamma)}\rangle$ can be evaluated separately for each γ , as shown in panel (b), by a Hadamard test like circuit. By measuring \hat{Z} at the ancilla qubit, we can evaluate $\text{Re}[\langle \Phi_{m-1}|\hat{\mathcal{P}}_{n}^{\alpha}\hat{\mathcal{P}}_{m}^{\alpha'}|\psi_{m+1}^{(\gamma)}\rangle]$ for $\theta=\pi/2$. A black circle in the circuits indicates a control qubit for a controlled unitary gate.

of the quantum circuit encoding algorithm is to find a quantum circuit $\hat{\mathcal{C}}$ that approximately represents $\hat{\Psi}$. Instead, here we assume that $|\Psi\rangle$ is given by a linear combination of quantum circuit states as in Eqs. (2) and (3). In this case, Eq. (33) can be more explicitly written as

$$\operatorname{Tr}_{\mathbb{I}_{m}}\left[\hat{\mathcal{F}}_{m}\hat{\mathcal{P}}_{i}^{\alpha}\hat{\mathcal{P}}_{j}^{\alpha'}\right] = \sum_{\gamma=1}^{\Gamma} \chi_{\gamma} \langle \Phi_{m-1} | \hat{\mathcal{P}}_{i}^{\alpha}\hat{\mathcal{P}}_{j}^{\alpha'} | \psi_{m+1}^{(\gamma)} \rangle \quad (34)$$

$$= \sum_{\gamma=1}^{\Gamma} \chi_{\gamma} \operatorname{Tr}_{\mathbb{I}_{m}} \left[\hat{f}_{m}^{(\gamma)} \hat{\mathcal{P}}_{i}^{\alpha} \hat{\mathcal{P}}_{j}^{\alpha'} \right], \tag{35}$$

where $\hat{f}_m^{(\gamma)}$ and $|\psi_{m+1}^{(\gamma)}\rangle$ are defined in Eqs. (24) and (25), respectively. As shown in Fig. 2(b), $f_{\alpha,\alpha'}^{(\gamma)} = \text{Tr}_{\mathbb{I}_m}[\hat{f}_m^{(\gamma)}\hat{\mathcal{P}}_i^{\alpha}\hat{\mathcal{P}}_j^{\alpha'}]$ can now be evaluated separately for each γ by using a Hadamard test like circuit on a quantum computer.

E. Initialization algorithm

Although the quantum circuit encoding algorithm described above in Sec. II C can be applied to general cases,

there are some exceptions for which care must be taken. For example, when we consider a ground state $|\Psi\rangle$ of a quantum spin system, the state $|\Psi\rangle$ is often in the spin singlet sector. In this case, there is no overlap between $|\Psi\rangle$ and $|0\rangle$ because the product state $|0\rangle$ represents the fully polarized state with the maximum spin value. Therefore, an alternative algorithm is required to construct an initial circuit $\hat{\mathcal{C}}$, for which $\hat{\mathcal{C}}^\dagger |\Psi\rangle$ has a finite overlap with $|0\rangle$.

Let us consider the reduced density matrix $\hat{\rho}$ of a quantum state $|\Psi\rangle$ on the subsystem $\mathbb{I} = \{i_1, i_2, \dots, i_K\}$ that is given by

$$\hat{\rho} = \text{Tr}_{\bar{1}}[|\Psi\rangle\langle\Psi|],\tag{36}$$

with the associated eigenstates and eigenvalues being denoted as $|\lambda_n\rangle$ and λ_n , respectively. Here we assume that λ_n is in the descending order, i.e., $\lambda_0 \geqslant \lambda_1 \geqslant \lambda_2 \geqslant \cdots$. The reduced density matrix $\hat{\rho}$ is then represented as

$$\hat{\rho} = \sum_{n} |\lambda_n \rangle \lambda_n \langle \lambda_n |. \tag{37}$$

We shall now find the unitary operator $\hat{\mathcal{V}}_1$ in the subsystem \mathbb{I} such that

$$\max_{\hat{\mathcal{V}}_1} \langle 0 | \hat{\mathcal{V}}_1^{\dagger} \hat{\rho} \hat{\mathcal{V}}_1 | 0 \rangle, \tag{38}$$

where $|0\rangle = |0\rangle_{i_1} |0\rangle_{i_2} \cdots |0\rangle_{i_K}$ in the computational basis defined in the subsystem \mathbb{I} with $1 \leqslant i_1 < i_2 < \cdots < i_K \leqslant L$.

For this end, let us first expand $\hat{\mathcal{V}}_1$ in the following general form:

$$\hat{V}_1 = \sum_{l=0}^{2^K - 1} \sum_{n=0}^{2^K - 1} v_{ln} |\lambda_l\rangle\langle n|,$$
 (39)

where $\{|n\rangle=|\sigma_{i_1}\sigma_{i_2}\cdots\sigma_{i_k}\rangle\}_{n=0}^{2^K-1}$ are the basis states in the subsystem \mathbb{I} and $n=\sum_{k=1}^K 2^{k-1}\sigma_{i_k}$. Because $\hat{\mathcal{V}}_1$ is unitary, $\sum_n v_{ln}v_{l'n}^*=\delta_{ll'}$ and $\sum_l v_{ln}^*v_{ln'}=\delta_{nn'}$. We then find that

$$\langle 0|\hat{\mathcal{V}}_{1}^{\dagger}\hat{\rho}\hat{\mathcal{V}}_{1}|0\rangle = \sum_{l=0}^{2^{K}-1} \lambda_{l}|v_{l0}|^{2} \leqslant \lambda_{0}. \tag{40}$$

It is now easy to find that

$$\hat{\mathcal{V}}_1 = \sum_{n=0}^{2^K - 1} |\lambda_n\rangle\langle n| \tag{41}$$

yields one of the solutions for Eq. (38). Once we determine the unitary operator \hat{V}_1 in Eq. (41), we can assign quantum gates for this operator by following the prescription described in Appendix A for the two-qubit case, if it is required.

In numerical simulations, we can determine \hat{V}_1 in Eq. (41) by directly evaluating the eigenstates $|\lambda_n\rangle$ of the reduced density operator $\hat{\rho}$. \hat{V}_1 can also be determined via a quantum computer. To show this, let us consider the subsystem \mathbb{I} composed of two qubits $\mathbb{I} = \{i, j\}$, for simplicity. Expanding the reduced density matrix $\hat{\rho}$ with a polynomials of the Pauli and identity operators

$$\hat{\rho} = \sum_{\alpha,\alpha'} \tilde{r}_{\alpha,\alpha'} \hat{\mathcal{P}}_i^{\alpha} \hat{\mathcal{P}}_j^{\alpha'}, \tag{42}$$

we find that

$$\langle \Psi | \hat{\mathcal{P}}_{i}^{\alpha} \hat{\mathcal{P}}_{j}^{\alpha'} | \Psi \rangle = \text{Tr}_{\mathbb{I}} \left[\hat{\rho} \hat{\mathcal{P}}_{i}^{\alpha} \hat{\mathcal{P}}_{j}^{\alpha'} \right] = 2^{2} \tilde{r}_{\alpha,\alpha'}. \tag{43}$$

This implies that the matrix elements $\tilde{r}_{\alpha,\alpha'}$ of $\hat{\rho}$ in Eq. (42) can be determined by measuring all possible pairs of products of the Pauli and identity operators $\hat{\mathcal{P}}_i^{\alpha}\hat{\mathcal{P}}_j^{\alpha'}$ ($\alpha,\alpha'=0,1,2,3$). This can be performed on a quantum computer directly if the state $|\Psi\rangle$ is given in a quantum circuit, or by using the procedure described in Sec. II D (also see Fig. 2), otherwise. Having estimated the reduced density matrix for $\hat{\rho}$, one can determine the unitary operator $\hat{\mathcal{V}}_1$ in Eq. (41) classically. The extension to the subsystem \mathbb{I} composed of more than two qubits is straightforward. We should also note that constructing a reduced density matrix by measuring a set of Pauli and identity operators on a quantum computer is known as quantum state tomography [52], and the technique described in Sec. II D is also along this line.

This procedure can be easily extended for further adding unitary operators $\hat{\mathcal{V}}_2, \hat{\mathcal{V}}_3, \ldots$. Let us assume that we have already determined the first unitary operator $\hat{\mathcal{V}}_1$ acting on $\mathbb{I} = \{i_1, i_2, \cdots, i_K\}$. The location of these qubits is selected among a set of clusters of K qubits $\mathbb{C} = \{\mathbb{I}_1, \mathbb{I}_2, \cdots, \mathbb{I}_C\}$ to maximize Eq. (38), i.e.,

$$\max_{\mathbb{I} \in \mathbb{C}} [\max_{\hat{\mathcal{V}}_1} \langle 0 | \hat{\mathcal{V}}_1^{\dagger} \hat{\rho} \hat{\mathcal{V}}_1 | 0 \rangle]. \tag{44}$$

Let us now define a quantum state $|\tilde{\Psi}_1\rangle$ incorporating $\hat{\mathcal{V}}_1^{\dagger}$ into the quantum state $|\Psi\rangle$, i.e.,

$$|\tilde{\Psi}_1\rangle = \hat{\mathcal{V}}_1^{\dagger} |\Psi\rangle,\tag{45}$$

and consider the reduced density matrix $\hat{\rho}_1$ of $|\tilde{\Psi}_1\rangle$ on the subsystem $\mathbb{I}' = \{i'_1, i'_2, \dots, i'_K\}$ given by

$$\hat{\rho}_1 = \text{Tr}_{\bar{\mathbb{I}}'}[|\tilde{\Psi}_1\rangle\langle\tilde{\Psi}_1|]. \tag{46}$$

 $\hat{\mathcal{V}}_2$ is then determined by maximizing $\langle 0|\hat{\mathcal{V}}_2^{\dagger}\hat{\rho}_1\hat{\mathcal{V}}_2|0\rangle$, i.e.,

$$\max_{\mathbb{I}' \in \mathbb{C}} \left[\max_{\hat{\mathcal{V}}_2} \langle 0 | \hat{\mathcal{V}}_2^{\dagger} \hat{\rho}_1 \hat{\mathcal{V}}_2 | 0 \rangle \right]. \tag{47}$$

This procedure can be continued until the desired number M_0 of unitary operators $\hat{\mathcal{V}}_1, \hat{\mathcal{V}}_2, \dots, \hat{\mathcal{V}}_{M_0}$ are added, i.e., $\hat{\mathcal{V}}_{M_0}^{\dagger} \cdots \hat{\mathcal{V}}_2^{\dagger} \hat{\mathcal{V}}_1^{\dagger} | \Psi \rangle$. Note that the reduced density operators $\hat{\rho}_1, \hat{\rho}_2, \dots$ can be evaluated on a quantum computer by the quantum state tomography. Algorithm 4 summarizes the procedure described above. Here, we generally assume the most general case of a set of clusters of K qubits $\mathbb{C} = \{\mathbb{I}_1, \mathbb{I}_2, \dots, \mathbb{I}_C\}$, but in practice we can simply consider a set of bonds of two qubits $\mathbb{B} = \{\mathbb{I}_1, \mathbb{I}_2, \dots, \mathbb{I}_B\}$.

F. Automatic quantum circuit encoding algorithm

Finally, we combine a prototype algorithm of the quantum circuit encoding, Algorithm 3, described in Sec. II C (also see Fig. 1) and the initialization algorithm, Algorithm 4, explained in Sec. II E, to automatically construct an optimal quantum circuit for encoding a give quantum state. The resulting algorithm is summarized in Algorithm 5 and is referred to as automatic quantum circuit encoding (AQCE) algorithm, which is schematically depicted in Fig. 3.

The AQCE algorithm is composed of two steps, i.e., the enlargement step in Figs. 3(b) and 3(c), and the optimization step in Fig. 3(d). The inputs of the AQCE algorithm are a target quantum state $|\Psi\rangle$, a quantum circuit $\hat{\mathcal{C}}$ set to be the identity operator \hat{I} , and a set of bonds \mathbb{B} of two qubits (and

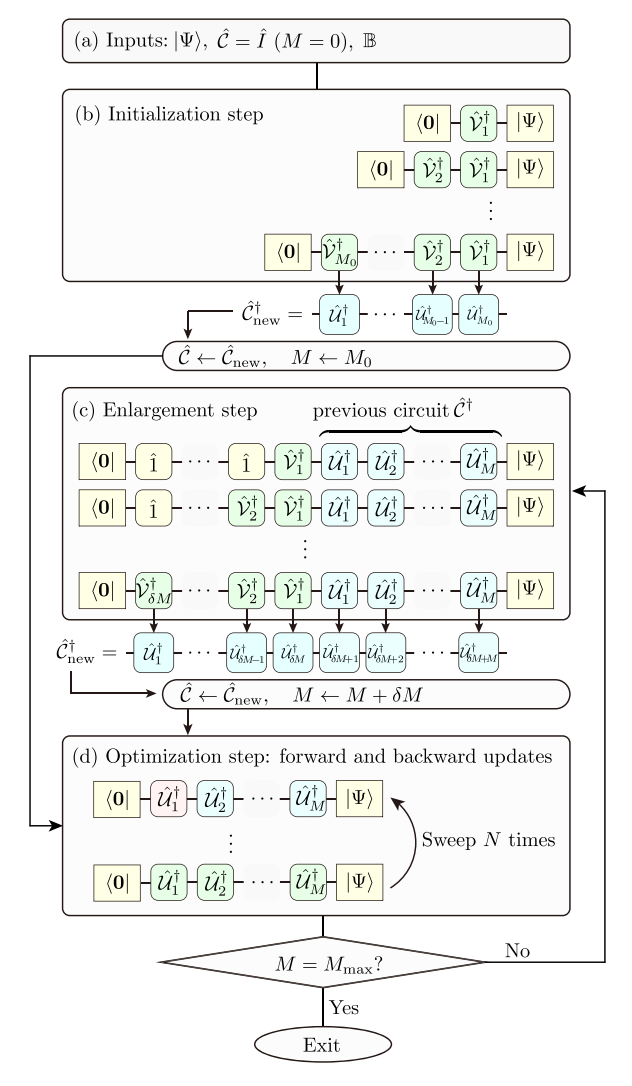


FIG. 3. Automatic quantum circuit encoding (AQCE) algorithm. (a) Inputs: a quantum states $|\Psi\rangle$, a quantum circuit \hat{C} , and a set of bonds \mathbb{B} of two quabits on which unitary operators act. We set $\hat{\mathcal{C}} = \hat{I}$ and thus the number M of unitary operators in the circuit is zero. (b) Initialization step. The initialization algorithm (Algorithm 4) is employed to properly construct M_0 unitary operators. (c) Enlargement step. δM unitary operators acting on two qubits (all set to the identity operators) are newly inserted in the circuit and the backward update algorithm (Algorithm 2) is applied only to these inserted δM unitary operators. (d) Optimization step. The circuit consisting of M unitary operators is optimized by the forward and backward updates N times (Algorithm 3), in which each unitary operator is updated one by one, including the location of qubits that the unitary operator acts on. The overall iteration is terminated when M reaches to the desired number M_{max} of unitary operators. Otherwise, the algorithm goes back to the enlargement step (c) and inserts additional δM unitary operators. The enlargement step (c) outputs the new quantum circuit \hat{C}_{new} with $M + \delta M$ unitary operators and this circuit is used as the input of the optimization step (d). Light-green and light-red boxes with rounded corners indicate updated unitary operators, while lightblue boxes with rounded corners indicate input unitary operators. The control parameters in the AQCE algorithm are M_0 , M_{max} , δM , and N.

ALGORITHM 4. Initialization algorithm.

```
Input Target state |\Psi\rangle, a set of clusters of K-qubits
   = \{\mathbb{I}_1, \mathbb{I}_2, \cdots, \mathbb{I}_C\}, and integer M_0
         Output Initialized quantum circuit \hat{C} = \hat{V}_1 \hat{V}_2 \cdots \hat{V}_{M_0}
         function Init|\Psi\rangle, \mathbb{C}, M_0
 2:
               Set |\tilde{\Psi}\rangle := |\Psi\rangle, \hat{\mathcal{C}} = \hat{I}
 3:
               for m = 1, 2, \dots, M_0 do
                      Evaluate matrix \mathbf{R}^{(k)} of the reduced density
 4:
        operator \hat{\rho}^{(k)} = \operatorname{Tr}_{\bar{\mathbb{I}}_k}[|\tilde{\Psi}\rangle\langle\tilde{\Psi}|] for all \mathbb{I}_k \in \mathbb{C}
                      Diagonalize \mathbf{R}^{(k)} = \mathbf{\Lambda}^{(k)} \operatorname{diag}(\lambda_0^{(k)}, \lambda_1^{(k)}, \cdots)(\mathbf{\Lambda}^{(k)})^{\dagger}
 5:
        with the lth eigenstate |\lambda_l^{(k)}\rangle and find k = k^* that
        maximizes \lambda_0^{(k)} among k = 1, 2, \dots, C
                      Set V := \sum_{n=0}^{2^K - 1} |\lambda_n^{(k^*)}\rangle \langle n| and assign the quantum
 6:
        gates for the unitary operator \hat{V}_m, represented by the
        matrix V, acting on \mathbb{I}_{k^*}.
                      Set \hat{\mathcal{C}} := \hat{\mathcal{C}}\hat{\mathcal{V}}_m, |\tilde{\Psi}\rangle := \hat{\mathcal{V}}_m^{\dagger}|\tilde{\Psi}\rangle.
 7:
            end for
 8:
            return \hat{\mathcal{C}}
 9:
10: end Function
```

a set of clusters $\mathbb C$ of K qubits, but here we assume that it is exactly the same set of bonds $\mathbb B$, for simplicity), as shown in Fig. 3(a). In the first enlargement step, we employ the initialization algorithm (Algorithm 4) as in Fig. 3(b) to construct a quantum circuit $\hat{\mathcal C}$ having M_0 number of unitary operators and finite overlap between $\hat{\mathcal C}|0\rangle$ and $|\Psi\rangle$. Then, in the following optimization step, we perform the forward and backward updates of the quantum circuit encoding algorithm (Algorithm 3) to optimize these unitary operators as in Fig. 3(d). The total number of sweeps for the optimization is set to N.

Next, we enlarge the quantum circuit by increasing the number M of unitary operators by δM , i.e., $M=M_0+\delta M$, as in Fig. 3(c). This is done by inserting δM identity operators next to $|0\rangle$ and perform the backward update of the quantum circuit encoding algorithm (Algorithm 2) to optimize these inserted δM unitary operators. We then move to the optimization step and perform the forward and backward

 $\label{eq:ALGORITHM} ALGORITHM 5. \ Automatic \ quantum \ circuit \ encoding \ (AQCE) \ algorithm.$

```
Input Target state |\Psi\rangle, integers (M_0, \delta M, M_{\text{max}}, N), and a set
of bonds \mathbb B
          Output Optimal quantum circuit \hat{C}
          function AQCE|\Psi\rangle, \mathbb{B}, M_0, \delta M, M_{\text{max}}, N
  1:
  2:
                 \hat{\mathcal{C}} := \text{INIT}(|\Psi\rangle, \mathbb{B}, M_0)
  3:
                 \hat{\mathcal{C}} := \text{SWEEP}(|\Psi\rangle, \hat{\mathcal{C}}, \mathbb{B}, N)
                 for M = M_0 + \delta M, M_0 + 2\delta M, \dots, M_{\text{max}} do
  4:
                        Set |\Psi'\rangle := \hat{\mathcal{C}}^{\dagger}|\Psi\rangle, \hat{\mathcal{C}}' = \hat{I}^{\delta M}
  5:
                        \hat{\mathcal{C}}' := \text{BACKWARD}(|\Psi'\rangle, \hat{\mathcal{C}}', \mathbb{B})
  6:
                        Set \hat{C} := \hat{C}\hat{C}'
  7:
                        \hat{\mathcal{C}} := \text{SWEEP}(|\Psi\rangle, \hat{\mathcal{C}}, \mathbb{B}, N)
  8:
  9:
              end for
            return \hat{\mathcal{C}}
10:
11: end Function
```

updates again (Algorithm 3) to optimize the whole M unitary operators as in Fig. 3(d). Notice that expect for the initial enlargement step, we perform in the enlargement step the backward update of the quantum circuit encoding algorithm (Algorithm 2), which is more efficient than the initialization algorithm (Algorithm 4). We repeat this whole iteration of the enlargement and optimization steps until the quantum circuit contains the desired number $M_{\rm max}$ of unitary operators. The control parameters in the AQCE algorithm are thus M_0 , $M_{\rm max}$, δM , and N.

Let us now briefly discuss the computational complexity. At each update of the unitary operator \hat{U}_m , we have to evaluate the fidelity tensor operator $\hat{\mathcal{F}}_m^{(k)}$ for B different bonds $\mathbb{I}_k \in \mathbb{B} = \{\mathbb{I}_1, \mathbb{I}_2, \cdots, \mathbb{I}_B\}$. The computational complexity of $\hat{\mathcal{F}}_m^{(k)}$ for a given single bond \mathbb{I}_k is proportional to the total number M of unitary operators in the quantum circuit when a quantum computer is used. Since there are 2M unitary operators to be updated at each sweep (i.e., one series of forward and backward updates), the total computational complexity for a single sweep is proportional to $2M^2B$. Therefore, if we assume that B as well as M is proportional to the number L of qubits, the total computational complexity is $O(L^3)$.

In contrast, if we perform the same calculation on a classical computer with the state-vector method, then the computational complexity of $\hat{\mathcal{F}}_m^{(k)}$ for given m and k is proportional to $2^{L-2}\times 16$, where the factor 16 is due to the number of matrix elements for $\hat{\mathcal{F}}_m^{(k)}$ and the factor 2^{L-2} is for the calculation of the overlap between two 2^{L-2} -dimensional state vectors. Therefore, the total computational complexity for a single sweep is proportional to $2^{L+3}MB$ and thus it becomes $O(2^{L+3}L^2)$ if we assume that B as well as M is proportional to the number L of qubits.

For comparison, we note that the computational complexity of the exact state preparation method proposed in Ref. [54] is $O(2^L)$. Therefore, no gain is expected in computational complexity for our algorithm when the state-vector method is employed on a classical computer. However, we should emphasize that the exact state preparation method in Ref. [54] generates a quantum circuit composed of $2^L - L - 1$ controlled-NOT gates and $2^L - L/2 - 1$ single-qubit gates. In contrast, in the AQCE algorithm, the number M of unitary operators is an input parameter and an optimal quantum circuit might be found with a reasonable accuracy even when $M \ll 2^L$.

In terms of the optimization method, one of the features in the AQCE algorithm is that the fidelity introduced as the cost function always monotonically increases after every update of unitary operators, simply because a better unitary operator is always adopted. This is in contrast to various gradient-based methods where the fidelity might decrease, depending on the size of the learning rate, i.e., a step size used to update a unitary operator. Since it is generally difficult to discuss analytically whether one heuristic method is better than other heuristic ones, we shall examine the performance of different methods numerically in the next section.

III. NUMERICAL SIMULATION

In this section, we demonstrate by numerical simulations the AQCE algorithm for quantum many-body states and for classical data. In particular, the latter application is potentially useful for quantum machine learning in preparing an input quantum state that represents classical data [55]. For the purpose of demonstration, we consider the unitary operators $\{\hat{\mathcal{U}}_m\}$ acting on two qubits. However, the AQCE algorithm can also be applied to general cases for K qubits with K > 2.

A. Quantum circuit encoding of quantum many-body states

Here, we show the numerical demonstration of the quantum circuit encoding for the ground states of the one-dimensional spin S=1/2 isotropic antiferromagnetic Heisenberg model and XY model. The Hamiltonian of these models is given as

$$\hat{\mathcal{H}} = \sum_{i=1}^{L} (\hat{X}_i \hat{X}_{i+1} + \hat{Y}_i \hat{Y}_{i+1} + \Delta \hat{Z}_i \hat{Z}_{i+1}), \tag{48}$$

where \hat{X}_i , \hat{Y}_i , and \hat{Z}_i are the x-, y-, and z-components of Pauli operators, respectively, at site i on a one-dimensional chain with L sites under periodic boundary conditions, i.e., $\hat{X}_{L+1} = \hat{X}_1$, $\hat{Y}_{L+1} = \hat{Y}_1$, and $\hat{Z}_{L+1} = \hat{Z}_1$. The Hamiltonian $\hat{\mathcal{H}}$ with $\Delta = 1$ and 0 corresponds to the isotropic Heisenberg and XY models, respectively, and the ground states of these two models are at criticality with algebraically decaying correlation functions.

The ground states $|\Psi\rangle$ of these models are calculated numerically by the standard Lancozs method within the accuracy of the ground state energy 10⁻¹². Although the AQCE algorithm is formulated deterministically, it turns out that the resulting structure of the quantum circuit depends on the numerical tiny error of the quantum state $|\Psi\rangle$ obtained by finite precision arithmetic. This is simply because even when the fidelity tensor $\hat{\mathcal{F}}_m$ for equivalent pairs of qubits is exactly the same theoretically, a particular pair of qubits $\mathbb{I} = \{i, j\}$ may be selected because of the numerical error due to finite precision calculations. Therefore, here we perform 100 AQCE calculations for each system size L, in which the ground state $|\Psi\rangle$ is prepared by the Lanczos method with 100 different initial Lanczos vectors, thus implying that the ground state $|\Psi\rangle$ to be encoded is slightly different numerically among these 100 different calculations, and select the best circuit $\hat{\mathcal{C}}$ in terms of the absolute value of the fidelity F given in Eq. (5). In addition, we perform 1000 sweeps to further optimize the unitary operators in the best circuit using the quantum circuit encoding algorithm (Algorithm 3). for the **AQCE** algorithm parameters $(M_0, N, \delta M, M_{\text{max}}) = (L, 20, L/2, L(L-5)/2)$ for the XY model and $(M_0, N, \delta M, M_{\text{max}}) = (L, 20, L/2, L^2/2)$ for the isotropic Heisenberg model. We set that a set of bonds $\mathbb B$ is composed of all pairs of two sites (i.e., qubits) $\{i, j\}$ with $i, j \in \mathbb{L}$, thus including pairs of distant sites.

Figure 4 shows the fidelity per site between the ground state $|\Psi\rangle$ of the XY model and the quantum circuit state $\hat{C}|0\rangle$ obtained by the AQCE algorithm. Here we use the fidelity per site rather than the fidelity itself because it is better suited for comparing results of different system sizes together, including the thermodynamic limit, which is similar to the energy per site being considered rather than the energy

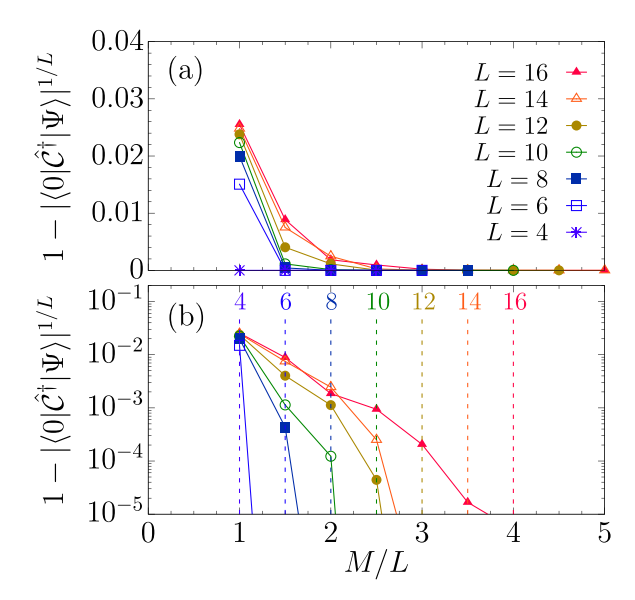


FIG. 4. (a) Fidelity per site between the ground state $|\Psi\rangle$ of the one-dimensional S=1/2 XY model and the quantum circuit state $\hat{\mathcal{C}}|0\rangle$ optimized by the AQCE algorithm for different system sizes L. (b) Semilog plot of panel (a). Vertical dashed lines with numbers in panel (b) indicate the number of local two-qubit unitary operators, $M_e=L^2/4$, required to represent the exact ground state by the DQAP ansatz [57].

itself [56]. We should first recall the previous results by the discretized quantum adiabatic process (DQAP) ansatz [57], a similar approach to digitized adiabatic quantum computing reported in Refs. [58,59], where a parametrized quantum circuit with brick-wall type structure is constructed on the basis of digitized quantum adiabatic process expressed by a product of local time-evolution unitary operators and the variational parameters are optimized to minimize the expectation value of energy, as in the variational quantum eigensolver (VQE) [2]. It is found in Ref. [57] that the optimized DQAP ansatz gives the exact ground state of the XY model with the minimum number $M_e = L^2/4$ of local two-qubit unitary operators set by the Lieb-Robinson bound for the brick-wall type structure. For comparison, this number M_{ℓ} is also indicated for each system size L in Fig. 4(b). We find that the AQCE algorithm can generate the quantum circuit state $\hat{\mathcal{C}}|0\rangle$ that represents essentially the exact ground state $|\Psi\rangle$ with $M=M_e$ for all system sizes studied except for L = 16, for which the convergence of the quantum circuit state $\hat{C}|0\rangle$ toward the ground state $|\Psi\rangle$ appears slower with increasing M. However, we should note that the quantum circuit state $\hat{C}|0\rangle$ with $M < M_e$ is better in terms of the fidelity than the DQAP ansatz composed of the same number M of local time-evolution unitary operators even for L = 16 [see Fig. 8(a)].

Figure 5 shows the fidelity per site between the ground state $|\Psi\rangle$ of the S=1/2 isotropic antiferromagnetic Heisenberg model and the quantum circuit state $\hat{\mathcal{C}}|0\rangle$ obtained by the AQCE algorithm. For smaller systems with $L\leqslant 8$, the AQCE algorithm can construct a quantum circuit state $\hat{\mathcal{C}}|0\rangle$ that represents numerically exactly the ground state $|\Psi\rangle$ with a less number of M. For example, one of the resulting quantum circuits describing the ground state for L=6 is shown in

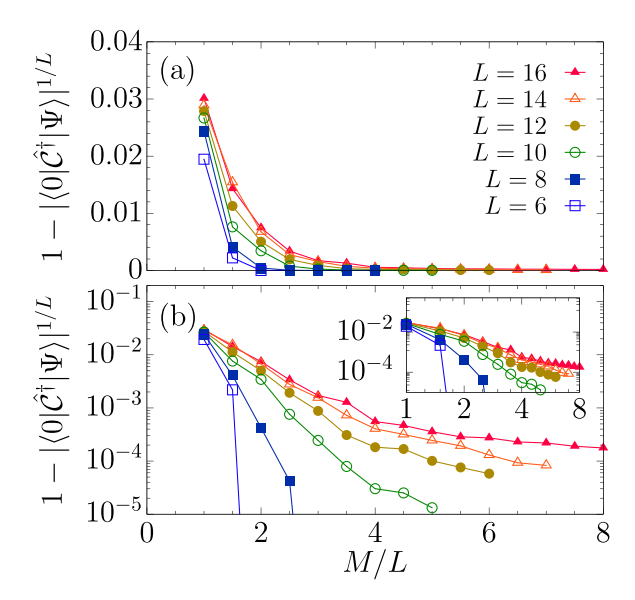
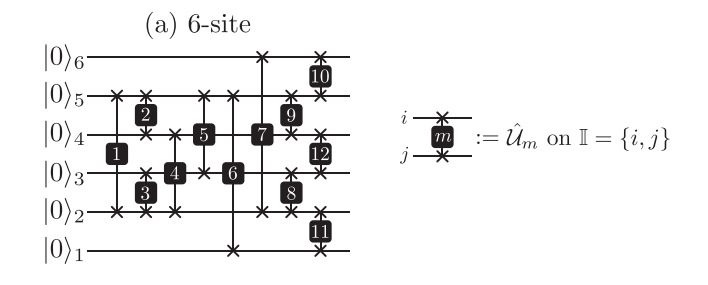


FIG. 5. Same as Fig. 4 but for the ground state $|\Psi\rangle$ of the one-dimensional S=1/2 isotropic antiferromagnetic Heisenberg model. The inset in panel (b) is the same plot but in a log-log scale.

Fig. 6(a). The number M of two-qubit unitary operators contained in this particular circuit is M = 12 and the number of independent real parameters, once these unitary operators are represented by a standard set of quantum gates (see Fig. 16), is $9 \times 12 + 3 \times 6 = 126$ if we combine adjacent two singlequbit Euler rotations into a single-qubit Euler rotation. In contrast, the dimension of the Hilbert space for the L=6system is $2^L = 64$, suggesting that there are 128 - 2 = 126independent real parameters, where two is subtracted because of the overall phase factor and the normalization factor. It is hence interesting to find that the number of the independent real parameters in this quantum circuit \hat{C} with M=12 coincides with that for the Hilbert space on which the quantum state $|\Psi\rangle$ is defined. However, it is highly nontrivial whether the quantum circuit \hat{C} composed of the limited number of two-qubit unitary operators can always represent any quantum state whenever the number of parameters in a quantum circuit is the same as that for the Hilbert space.

We should also note that the two-qubit unitary operators in the optimized quantum circuit $\hat{\mathcal{C}}$, representing the ground state $|\Psi\rangle$ essentially exactly for L=6 and 8 (see Fig. 5), are not uniformly distributed, as shown in Fig. 6, even though the ground state $|\Psi\rangle$ represented by the quantum circuit is translational symmetric (apart from the finite precision numerical error). Figure 6(b) shows one of the resulting quantum circuits describing the ground state for L=8. The circuit structure is much more complicated than that for L=6 shown in Fig. 6(a). Nonetheless, we have confirmed numerically that the resulting quantum circuit states $\hat{\mathcal{C}}|0\rangle$ for L=6 and 8 are essentially translational symmetric and also spin rotation symmetric.

In contrast, for the systems with L > 8, we find that the convergence of the optimized quantum circuit state $\hat{C}|0\rangle$ toward the ground state $|\Psi\rangle$ is slower with the number M of unitary operators, although the convergence is still



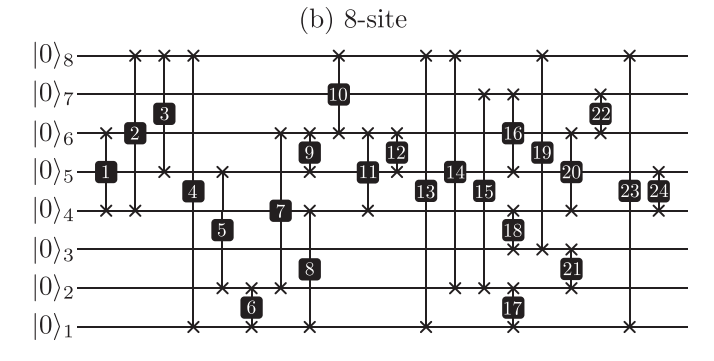


FIG. 6. Optimized quantum circuit states $\hat{C}|0\rangle$ obtained by the AQCE algorithm, which represent essentially exactly the ground states of the one-dimensional S=1/2 isotropic antiferromagnetic Heisenberg model for (a) L=6 and (b) L=8, containing 12 and 24 two-qubit unitary operators $\{\hat{\mathcal{U}}_m\}$, respectively, denoted by black squares with number m in them. The location of two qubits on which each unitary operator acts is indicated by crosses. Each two-qubit unitary operator can be decomposed into a standard set of quantum gates (see Fig. 16) with having 15 independent real parameters (apart from a single global phase). Since adjacent two single-qubit Euler rotations are combined into a single single-qubit Euler rotation, the total number of independent real parameters is 126 for L=6 in panel (a) and 240 for L=8 in panel (b).

approximately exponential, as shown in Fig. 5(b). For example, the error in fidelity of the optimized quantum circuit state $\hat{\mathcal{C}}|0\rangle$ for L=16 is still relatively large even when M/L=8. Moreover, we observe in Fig. 5(b) that the slope of the fidelity as a function of M in the semilog plot becomes more flattered with increasing the system size L. We speculate that this is due to a difficulty of sequentially optimizing each unitary operator $\hat{\mathcal{U}}_m$, including the location of qubits on which the unitary operator $\hat{\mathcal{U}}_m$ acts, when the system size is large.

In fact, previous studies in Refs. [60,61], which carefully designed quantum circuit structures suitable for representing the ground state of the one-dimensional Heisenberg model, found that the accuracy of the ground state energy improves linearly with the number of parameters in a logarithmic plot. In contrast, our results, shown in the inset of Fig. 5(b), deviate from this linear trend, specially in the region of a large number of gates, exhibiting a nearly flattened behavior for L=16. Therefore, from an optimization perspective, our method of automatically searching for an optimal quantum circuit encounters difficulties when dealing with larger system sizes. Since further systematic analysis of larger system sizes requires significantly more computational resources, we leave this issue for future study.

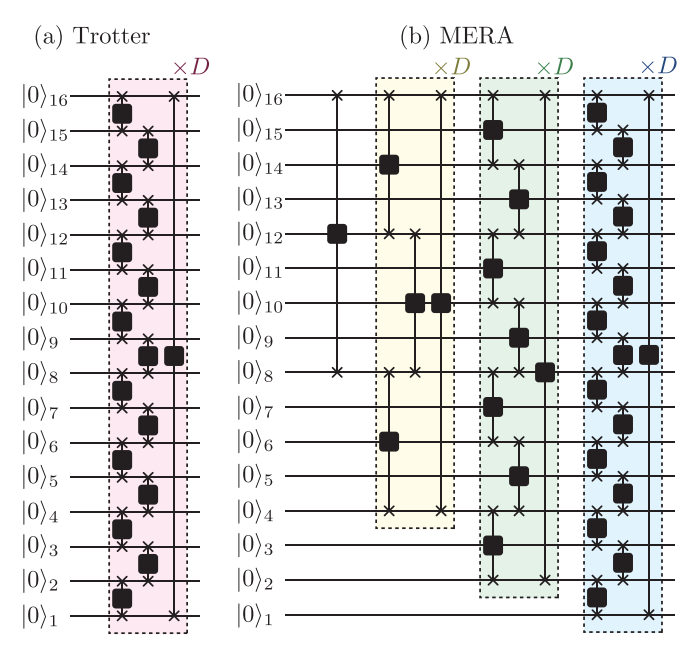


FIG. 7. (a) Trotter-like circuit and (b) MERA-like circuit for a 16-qubit system. Two-qubit unitary operators $\{\hat{\mathcal{U}}_m\}$ are indicated by back squares and the location of two qubits on which each unitary operator acts is indicated by crosses. Shaded color layers are repeated D times.

B. Quantum circuit encoding with fixed Trotterand MERA-like circuit structures

In this section, using numerical simulations, we shall compare the results obtained by the AQCE algorithm, which can automatically construct a quantum circuit with a self-assembled optimal structure, and those obtained for a quantum circuit with a fixed circuit structure. For this purpose, here we consider two particular fixed circuit structures. One is a Trotter-like circuit structure schematically shown in Fig. 7(a). In this Trotter-like circuit, two-qubit unitary operators $\{\hat{\mathcal{U}}_m\}$ acting on adjoining qubits are distributed as if a time evolution operator of the whole system is Trotter decomposed into two parts in a one dimensionally aligned qubit ring. The quantum circuit is composed of D layers and each layer corresponds to one Trotter step, containing L two-qubit unitary operators $\{\hat{\mathcal{U}}_m\}$. Therefore, the total number M of unitary operators $\{\hat{\mathcal{U}}_m\}$ in the Trotter-like circuit is DL.

The other circuit structure considered here is inspired by the MERA and is shown schematically in Fig. 7(b). In this MERA-like circuit, each basic layer indicated by different shaded color in Fig. 7(b) represents a different length scale and thus two-qubit unitary operators $\{\hat{\mathcal{U}}_m\}$ in different basic layers act on two qubits that are located in different (adjoining as well as distant) distances. To improve the accuracy, we also increase the number of layers in each basic layer D times [see Fig. 7(b)], and therefore the total number M of unitary operators $\{\hat{\mathcal{U}}_m\}$ in the MERA-like circuit is $D(L+L/2+L/2^2+L/2^3+\cdots+4)+(2-1)=2D(L-2)+1$, assuming that the system size L is factorial of 2. To optimize two-qubit unitary operators $\{\hat{\mathcal{U}}_m\}$ in the Trotter- and MERA-like circuits for encoding a quantum state $|\Psi\rangle$, we perform 1000 sweeps of the forward and

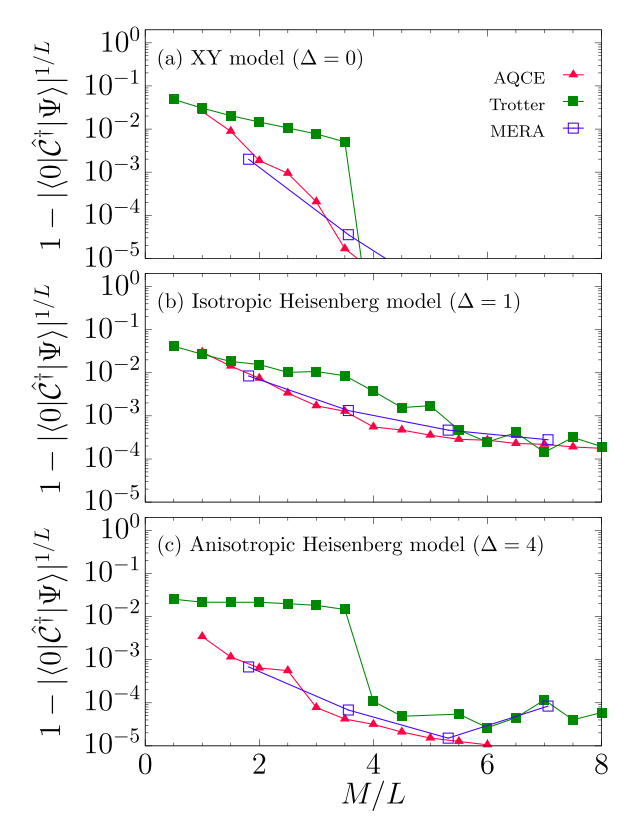


FIG. 8. (a) Fidelity per site between the ground state $|\Psi\rangle$ of the one-dimensional S=1/2 XY model and the quantum circuit states $\hat{\mathcal{C}}|0\rangle$ obtained by the AQCE algorithm and with the Trotter- and MERA-like circuit structures for L=16. (b) Same as panel (a) but for the ground state $|\Psi\rangle$ of the one-dimensional S=1/2 isotropic antiferromagnetic Heisenberg model. (c) Same as panel (a) but for the ground state $|\Psi\rangle$ of the one-dimensional S=1/2 anisotropic antiferromagnetic Heisenberg model with $\Delta=4$. The results obtained by the AQCE algorithm in panels (a) and (b) are the same as those shown in Figs. 4 and 5, respectively. Note that the ground states in panels (a) and (b) are at criticality, while the ground state in panel (c) is away from criticality.

backward updates sequentially (see Sec. II C), i.e., the quantum circuit encoding algorithm, but with the fixed circuit structure.

Figure 8(a) shows the fidelity per site between the ground state $|\Psi\rangle$ of the XY model and the optimized quantum circuit states $\mathcal{C}|0\rangle$ obtained by the AQCE algorithm and with the Trotter- and MERA-like circuit structures for L = 16. First, we find that the quantum circuit state with the Trotter-like circuit structure can represent numerically exactly the ground state $|\Psi\rangle$ at M=4L (corresponding to $L^2/4$ for L=16), which is consistent with the previous study using the DQAP ansatz [57]. This is understood simply because the Trotter-like circuit and the DQAP ansatz have the same circuit structure, although these two approaches employ different optimization schemes to determine the optimal two-qubit unitary operators: In the DQAP ansatz, each two-qubit unitary operator is parametrized with a single variational parameter [i.e., $\hat{\mathcal{D}}$ with $\alpha_1 = \alpha_2$ and $\alpha_3 = 0$ in Eq. (A4) for the XY model and the variational parameters are optimized to minimize the expectation value of energy, while the optimal unitary operators in the Trotter-like circuit are determined by maximizing the fidelity of the ground state in the quantum circuit encoding algorithm with the fixed circuit structure. We also find in Fig. 8(a) that the quantum circuit state $\hat{\mathcal{C}}|0\rangle$ obtained by the AQCE algorithm is much better than that with the Trotter-like circuit structure when M < 4L and it is competitive in terms of the accuracy with that with the MERA-like circuit structure.

Figure 8(b) shows the fidelity per site between the ground state $|\Psi\rangle$ of the isotropic antiferromagnetic Heisenberg model and the optimized quantum circuit states $\hat{C}|0\rangle$ obtained by the AQCE algorithm and with the Trotter- and MERA-like circuit structures for L=16. Similar to the results for the XY model in Fig. 8(a), the quantum circuit state $\hat{C}|0\rangle$ obtained by the AQCE algorithm exhibits the better accuracy than that with the Trotter-like circuit structure and it is compatible with that with the MERA-like circuit structure when $M\leqslant 5L$. However, for M>5L, all these three quantum circuit states show the similar accuracy that is improved approximately exponentially with increasing M.

The ground states in these two cases are both at criticality and the MERA is known to be best suited for describing such a quantum state [62]. Therefore, it is also interesting to study a case for which the ground state is away from criticality. Figure 8(c) shows the fidelity per site between the ground state $|\Psi\rangle$ of the anisotropic antiferromagnetic Heisenberg model with $\Delta = 4$ and the optimized quantum circuit states $\hat{C}|0\rangle$ obtained by the AQCE algorithm and with the Trotter- and MERA-like circuit structures for L = 16. In this case, the ground state is gapped and is less entangled as compared to those of the previous two models with $\Delta = 0$ and $\Delta = 1$. Therefore, one expects that the number of two-qubit unitary operators required to achieve given accuracy for $\Delta = 4$ is smaller than that for $\Delta = 0$ and $\Delta = 1$. We indeed find in Fig. 8(c) that the fidelity is much closer to 1 even when the number of two-qubit unitary operators is small for the optimized quantum circuit states obtained by the AOCE algorithm and with the MERA-like circuit structure, but not for the optimized quantum circuit state with the Trotter-like circuit structure. In the case of the Trotter-like circuit, the fidelity first remains almost constant with increasing M until M = 4Lat which the fidelity suddenly jumps to a larger value and then again remains almost constant afterward.

It is also interesting to observe in Figs. 8(b) and 8(c) that the fidelity becomes approximately independent of the quantum circuit structures employed when M/L is larger than 4 or 5. A possible reason for this is due to the effect of the barren plateau phenomena. It is known that the unitary 2-design can be realized in polynomial time (i.e., a polynomial number of layers of gates) for a quantum circuit where two-qubit unitary operators are randomly distributed [31]. As shown in Fig. 6(b), the distribution of two-qubit unitary operators in the quantum circuit obtained by the AQCE algorithm for L=8is quite random. Therefore, it is naturally expected that the quantum circuit obtained exhibits the unitary 2-design and thus might suffer from the barren plateaus phenomena. Since the fidelities for other quantum circuits also exhibit similar values, we expect that all of them might suffer from the barren plateau phenomena. Indeed, we find that in all cases, the change of the quantum circuit during the optimization iteration is very small when M is large. This implies that a better quantum circuit can be generated more efficiently when the number of two-qubit unitary operators is small enough not to exhibit the unitary 2-design. However, we should note that the small improvement of fidelity with further increasing M also simply implies trapping of a local minimum of the cost function. Additionally, we note that the two fixed circuit structures in Fig. 7 adopt a design where brick-wall type circuit structures are inserted to improve accuracy. However, as the total number of these brick-wall layers increases, the optimization is expected to become more difficult due to the loss of locality [25,63].

C. Comparison with parametrized quantum circuit encoding optimized by a gradient-based method

So far, we have demonstrated the quantum circuit encoding algorithm that can generate an optimal quantum circuit state $\hat{C}|0\rangle$ approximately representing a quantum state $|\Psi\rangle$. In this section, we compare numerically the results of the quantum circuit encoding algorithm with those obtained by a parametrized quantum circuit encoding algorithm in which the parameters are optimized with a gradient-based method.

In the conventional variational quantum algorithms such as the VQE algorithm [1–3], we consider a parametrized circuit $\hat{C}(\theta)$ and intend to minimize the expectation value $E(\theta)$ of an objective operator $\hat{\mathcal{H}}_o$,

$$E(\boldsymbol{\theta}) = \langle 0|\hat{\mathcal{C}}^{\dagger}(\boldsymbol{\theta})\hat{\mathcal{H}}_{o}\hat{\mathcal{C}}(\boldsymbol{\theta})|0\rangle, \tag{49}$$

for a set of real parameters $\theta = \{\theta_1, \theta_2, \dots, \theta_P\}$. Therefore, if we set the following objective operator:

$$\hat{\mathcal{H}}_o = 1 - |\Psi\rangle\langle\Psi|,\tag{50}$$

a quantum circuit $\hat{C}(\theta^*)$ with an optimized set of parameters θ^* can represent approximately a desired quantum state $|\Psi\rangle$, i.e., $|\Psi\rangle\approx\hat{C}(\theta^*)|0\rangle$. We refer to this algorithm as the parametrized quantum circuit encoding algorithm.

A standard technique to optimize the parameters θ is a gradient-based method and here we employ the natural gradient method [21]:

$$\boldsymbol{\theta}' = \boldsymbol{\theta} - \tau \mathbf{S}^{-1} \boldsymbol{f},\tag{51}$$

where θ' indicates the updated parameters, and S and f are a $(P \times P)$ matrix and a P-dimensional vector given by

$$(S)_{kk'} = \text{Re}\left(\langle 0|\frac{\partial \mathcal{C}^{\dagger}}{\partial \theta_k}\frac{\partial \mathcal{C}}{\partial \theta_{k'}}|0\rangle - \langle 0|\frac{\partial \mathcal{C}^{\dagger}}{\partial \theta_k}\mathcal{C}|0\rangle\langle 0|\mathcal{C}^{\dagger}\frac{\partial \mathcal{C}}{\partial \theta_{k'}}|0\rangle\right)$$
(52)

and

$$[f]_{k} = \operatorname{Re}\left(\langle 0|\frac{\partial \mathcal{C}^{\dagger}}{\partial \theta_{k}}\hat{\mathcal{H}}\mathcal{C}|0\rangle - \langle 0|\frac{\partial \mathcal{C}^{\dagger}}{\partial \theta_{k}}\mathcal{C}|0\rangle\langle 0|\mathcal{C}^{\dagger}\hat{\mathcal{H}}\mathcal{C}|0\rangle\right),\tag{53}$$

respectively. τ is a learning rate and we set $\tau=0.01$ in the following numerical demonstration. The quantum circuit structure used in the parametrized quantum circuit encoding algorithm is the Trotter-like circuit structure shown in Fig. 7(a) and each two-qubit unitary operator is assigned to a SU(4) gate that is composed of the elementary gates, i.e., three controlled-NOT gates and parametrized single-qubit gates, as shown in Fig. 16(c). Therefore, the total number M

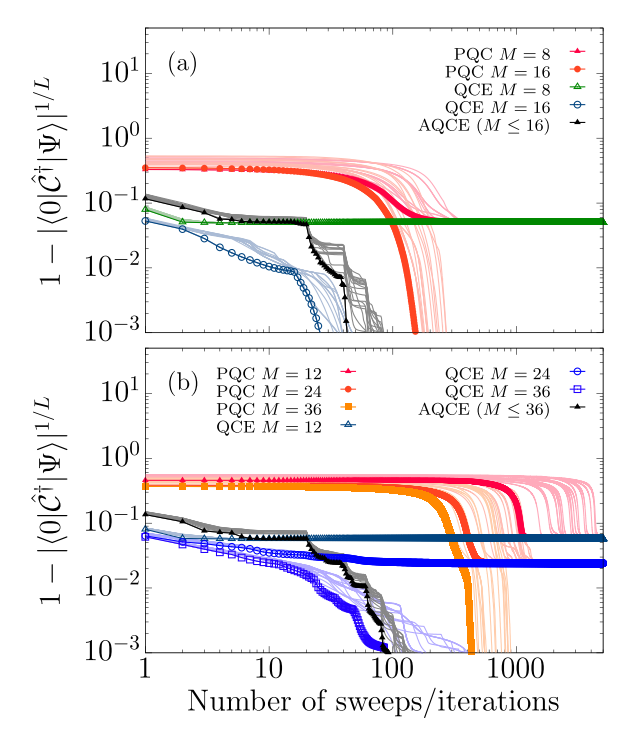


FIG. 9. Fidelity per site between the ground state $|\Psi\rangle$ of the one-dimensional S = 1/2 XY model and the optimized quantum circuit states $\hat{C}|0\rangle$ and $\hat{C}(\theta^*)|0\rangle$ obtained, respectively, by the AQCE algorithm (black lines and symbols, denoted as AQCE) and the parametrized quantum circuit encoding algorithm (colored lines and solid symbols, denoted as PQC) for (a) L = 8 and (b) L = 12. In the parametrized quantum circuit encoding algorithm, we adopt the Trotter-like circuit consisting of M two-qubit unitary operators [see Fig. 7(a)]. For comparison, we also show the results obtained by the quantum circuit encoding algorithm (colored lines and open symbols, denoted as PQC) with the same circuit structure employed in the parametrized quantum circuit encoding algorithm. The symbols represent the best results and the thin lines show the next 20 best results out of totally 100 independent simulations. In the AQCE calculations, we perform the enlargement procedure up to $M = L^2/4$ with $\delta M = L$ and N = 20, and continue the optimization step with the fixed M. The horizontal axis indicates the number of sweeps for the AQCE and the quantum circuit encoding algorithms, and the number of optimization iterations of the natural gradient method for the parametrized quantum circuit encoding algorithm. Note that a single iteration in the parametrized quantum circuit encoding algorithm updates all the parameters in the parametrized quantum circuit at once.

of the two-qubit unitary operators in the quantum circuit is M = DL and the total number P of the real parameters is P = 9M + 3L, assuming that adjacent two single-qubit Euler rotations are combined into a single single-qubit Euler rotation. As the initial condition for the optimization iteration in Eq. (51), all these parameters are chosen randomly.

Figure 9 (Fig. 10) shows the fidelity per site between the ground state $|\Psi\rangle$ of the S=1/2 XY model (isotropic antiferromagnetic Heisenberg model) and the optimized quantum circuit states $\hat{\mathcal{C}}|0\rangle$ and $\hat{\mathcal{C}}(\theta^*)|0\rangle$ obtained by the AQCE algorithm and the parametrized quantum circuit encoding algorithms, respectively, for L=8 and 12. In these numerical

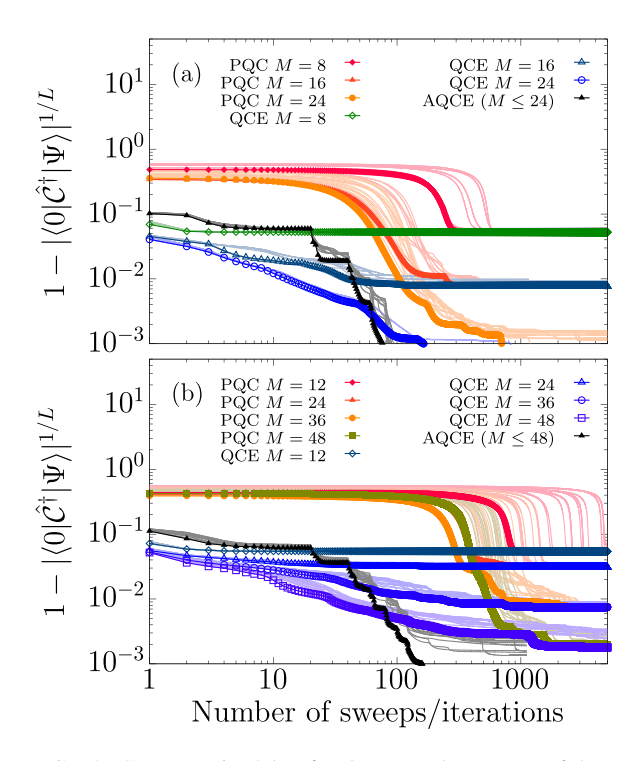


FIG. 10. Same as Fig. 9 but for the ground state $|\Psi\rangle$ of the one-dimensional S=1/2 isotropic antiferromagnetic Heisenberg model. In the AQCE calculation, we perform the enlargement procedure up to $M=L^2/4+L$ with $\delta M=L$ and N=20, and continue the optimization step with the fixed M.

simulations, we perform 100 independent simulations for each case and the best result (indicated by symbols) as well as the next 20 best results (indicated by thin lines) after the fixed amount of sweeps or iterations are shown in these figures. We also set $\mathbb B$ as the set of all possible pairs of qubits. Additionally, for comparison, we show the results obtained by applying the quantum circuit encoding algorithm to circuits of the same structure employed in the parameterized quantum circuit encoding algorithm.

First, by comparing the results obtained by the quantum circuit encoding algorithm and the parameterized quantum circuit encoding algorithm, as shown in Figs. 9 and 10, we observe a significant difference in fidelity from the very first iteration. Despite using the same circuit structure with each unitary operator initialized as the identity operator, the accuracy notably improves at the first iteration for the quantum circuit encoding algorithm. A similar improvement does not occur in the parameterized quantum circuit encoding algorithm because the derivative of the cost function around the identity matrix is close to zero, leading to an essentially negligible change in the variational parameters at the beginning of the iteration. One possible solution is to use a Haar random matrix instead of the identity matrix for the initial unitary matrix; however, this would exacerbate the barren plateau effect. Therefore, this initialization issue is a drawback of the gradient-based optimization method used in the parametrized quantum circuit encoding algorithm. In contrast, this issue is effectively avoided in the method using SVD, as employed in the quantum circuit encoding algorithm.

Next, in terms of the number of iterations required for the overall calculation, the AQCE and quantum circuit encoding algorithms, both of which use the optimization based on SVD, tend to converge faster that the parametrized quantum circuit algorithm. However, it is important to note that in the parameterized quantum circuit encoding algorithm, the convergence rate can be adjusted by increasing τ . Nevertheless, if this parameter τ is set too large, then the calculation might break down, necessitating careful tuning to find an optimal τ . In contrast, since the AQCE and quantum circuit encoding algorithms select the locally optimal solution, there is no need for such fine tuning, which is a significant advantage of these algorithms. Additionally, comparing the results obtained by the AQCE algorithm with those obtained by the quantum circuit encoding algorithm with a sufficient large number of unitary operators, there is no significant difference in the number of sweeps required to achieve convergence. Therefore, the AQCE algorithm is a convenient method for cases where an appropriate circuit structure is not know a priori. For instance, as shown in Fig. 9(b), in the XY model, all three algorithms can achieve high accuracy with a comparable number of twoqubit unitary operators. However, in the Heisenberg model shown in Fig. 10(b), the parameterized quantum circuit encoding algorithm and the quantum circuit encoding algorithm do not even reach an infidelity per site as small as 10^{-3} , even using 48 two-qubit unitary operators for L = 16. In contrast, the AQCE algorithm achieves an infidelity smaller than 10^{-3} with 48 two-qubit unitary operators for the same system size. The AQCE algorithm explores a better circuit structure, including long-range gates, resulting in a better quantum circuit state with the same number of two-qubit unitary operators. However, selecting an optimal circuit structure, such as one found here, is generally challenging.

D. Quantum circuit encoding of classical data

In this section, we demonstrate that the AQCE algorithm is also useful to construct an optimal quantum circuit to represent classical data such as a classical image. It is well known that there are several ways to encode classical data to a quantum state (for example, see Ref. [55]). However, it is usually not obvious how to optimally prepare such a quantum state encoding particular classical data in a quantum circuit with a less number of quantum gates. We show that the AQCE algorithm can be a promising approach for this purpose.

One way to express classical data in a quantum state is the amplitude encoding [64], where the classical data $x = \{x_0, x_1, \dots, x_n, \dots, x_{N-1}\}$ is described by using a quantum state

$$|\Psi_{\rm c}\rangle = \sum_{n=0}^{N-1} \bar{x}_n |n\rangle. \tag{54}$$

Here, $|n\rangle$ is the basis labeled by Eq. (1) with $L \ge \log_2 N$ and

$$\bar{x}_n = x_n / \sqrt{V_x},\tag{55}$$

with V_x being a volume of x given by

$$V_x = \sum_{n=0}^{N-1} |x_n|^2. (56)$$

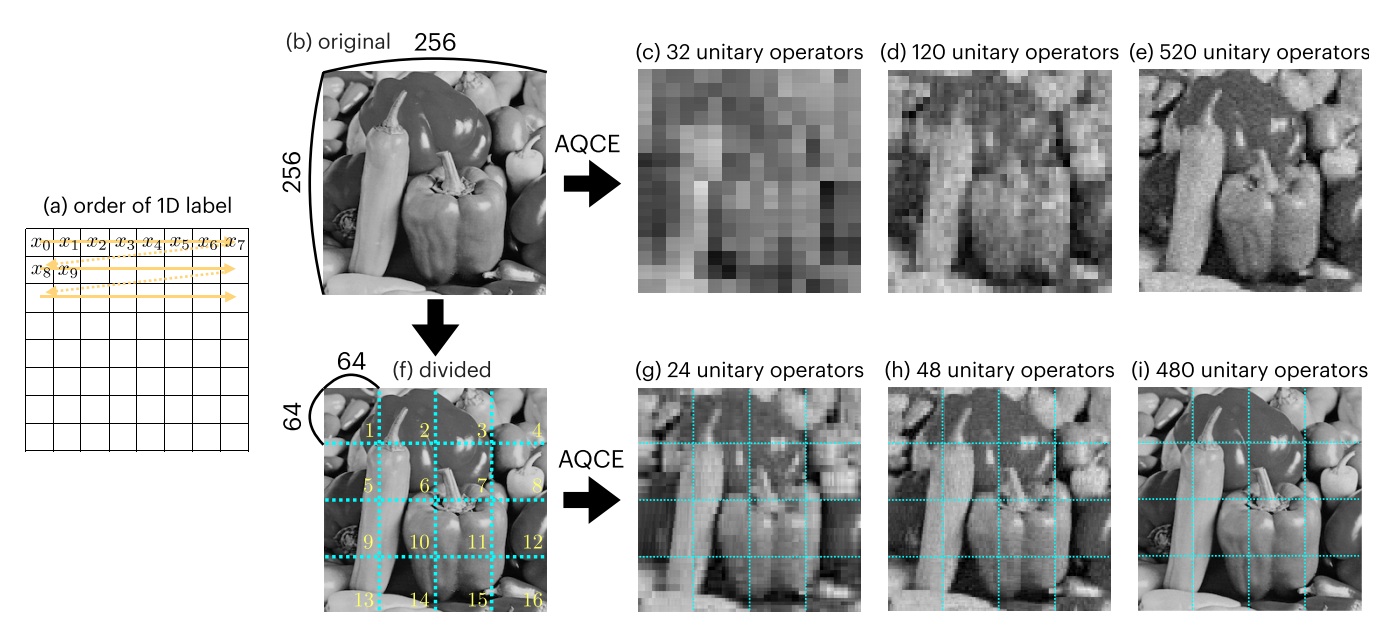


FIG. 11. Quantum circuit encoding of a gray scale picture known as "Peppers" [72]. (a) Labeling of two-dimensional classical data (with 8×8 pixels, as an example). (b) Original picture with 256×256 pixels. (c)–(e) Pictures reconstructed by decoding the quantum circuit states $\hat{C}|0\rangle$ on L=16 qubits with the different number M of two-qubit unitary operators, M=32, 120, and 520. (f) Original picture divided into 16 pieces ($m_s=1,2,\ldots,16$ indicated by yellow in the picture) with 64×64 pixels each. (g)–(i) Pictures reconstructed by decoding each quantum circuit state $\hat{C}^{(m_s)}|0\rangle$ on L=12 qubits with the different number M of two-qubit unitary operators, M=24, 48, and 480.

Each element x_n in the classical data x is usually real number, but the amplitude encoding can also be applied to the case of complex number. There exist several proposals to implement the amplitude encoding [65–68]. However, these are in general not best fit for a near-term application. A variational quantum algorithm using a parametrized quantum circuit has also been proposed recently [69–71].

In the previous sections, we have demonstrated the quantum circuit encoding of a quantum state focusing on the ground state of a typical many-body Hamiltonian encountered in condensed matter physics and quantum statistical physics, which is in some sense simple. Instead, a quantum state given in Eq. (54) representing classical data is relatively complicated and moreover there is no prior knowledge of such a quantum state. Therefore, the quantum circuit encoding of such a quantum state in Eq. (54) is generally a difficult task in any means. Here, we employ the AQCE algorithm to demonstrate the quantum circuit encoding of a quantum state representing a classical image.

As an example of a classical image, we consider the gray scale picture shown in Fig. 11(b), which is also known as "Peppers" available in Ref. [72]. The data size of this picture is 256×256 pixels and each pixel in the two-dimensional array is assigned to represent each part of the picture located at a position labeled (i_x, i_y) with $i_x = 0, 1, 2, \dots, 255$ (=2⁸ – 1) in the horizontal axis from left to right and $i_y = 0, 1, 2, \dots, 255$ in the vertical axis from top to bottom, as shown in Fig. 11(a). Therefore, the picture is fully given by a 2¹⁶ dimensional vector $\mathbf{x}_{\text{Pep}} = \{x_0, x_1, x_2, \dots, x_s, \dots, x_{65535}\}$ of nonnegative real numbers, where label $s = i_x + 256i_y$. This suggests that the data can be transformed into a quantum state $|\Psi_c\rangle$ in the form given in Eq. (54) with L = 16 qubits. Using numerical simulations, we perform the AQCE algorithm to encode the quantum state $|\Psi_c\rangle$ into an optimal quantum circuit

state $\hat{\mathcal{C}}|0\rangle$. For this end, we set the control parameters in the AQCE algorithm as $(M_0, N, \delta M) = (16, 100, 8)$ with varying the total number M of two-qubit unitary operators $\{\hat{\mathcal{U}}_m\}$ in the generated quantum circuit (defined as M_{max} in Sec. II F and also in Algorithm 5).

Figures 11(c)-11(e) show the reconstructed pictures by decoding the quantum circuit states $\hat{C}|0\rangle$ with the different number M of two-qubit unitary operators. In reconstructing the classical data $\mathbf{x}' = \{x'_0, x'_1, \dots, x'_n, \dots, x'_{N-1}\}$ from the amplitude $\bar{x}'_n = \langle n|\hat{\mathcal{C}}|0\rangle$ of the quantum circuit state, we have to rescale back the amplitude with the volume V_x , i.e., $x'_n =$ $\sqrt{V_r'}\bar{x}_n'$. It turns out that when the number M of two-qubit unitary operators is extremely small, the reconstructed picture looks more like a mosaic, as shown in Fig. 11(c) for M = 32. However, as expected, the reconstructed pictures are improved with increasing M [see Figs. 11(d) and 11(e)]. To be more quantitative, we plot the fidelity between the quantum state $|\Psi_{\rm c}\rangle$ representing the original picture and the quantum circuit state $\hat{C}|0\rangle$ in Fig. 12. The fidelity improves rather rapidly with increasing M for M up to 50, but the improvement becomes somewhat slower for M > 100.

For the better performance, next we simply divide the original classical data $\mathbf{x}_{\text{Pep}} = \{x_0, x_1, x_2, \cdots, x_{65535}\}$ into 16 pieces, each representing a 64 × 64 pixels picture, as shown in Fig. 11(f). This implies that each segment of the picture is given by a 2^{12} dimensional vector, i.e., $\mathbf{x}_{\text{Pep}}^{(m_s)} = \{x_0^{(m_s)}, x_1^{(m_s)}, x_2^{(m_s)}, \cdots, x_{4095}^{(m_s)}\}$ with $m_s = 1, 2, \ldots, 16$. Accordingly, a quantum state $|\tilde{\Psi}_c\rangle$ for the whole picture is given by a direct product of quantum states $|\tilde{\Psi}_c^{(m_s)}\rangle$ representing different segments of the original picture, i.e.,

$$|\tilde{\Psi}_{c}\rangle = \bigotimes_{m_{s}=1}^{16} |\Psi_{c}^{(m_{s})}\rangle, \tag{57}$$

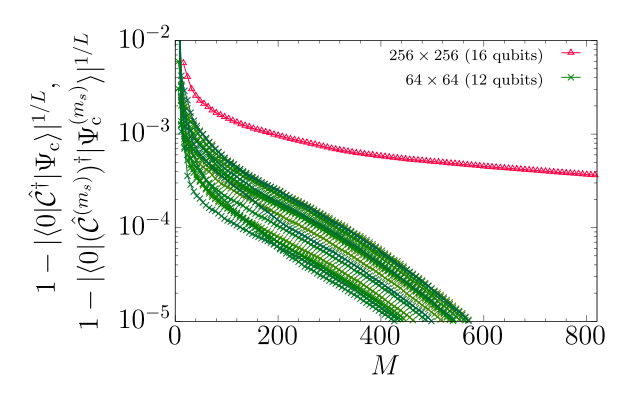


FIG. 12. Fidelity per site between the quantum state $|\Psi_c\rangle$ ($|\Psi_c^{(m_s)}\rangle$) on L=16 (L=12) qubits representing the original picture in Fig. 11(b) [the m_s th segment of the original picture in Fig. 11(f)] and the quantum circuit state $\hat{\mathcal{C}}|0\rangle$ ($\hat{\mathcal{C}}^{(m_s)}|0\rangle$) indicated by red triangles (green crosses). Here, $m_s=1,2,\ldots,16$ and thus 16 different results are shown for the case where the picture is divided into 16 pieces.

where

$$|\Psi_{c}^{(m_s)}\rangle = \sum_{n=0}^{2^{12}-1} \bar{x}_n^{(m_s)} |n^{(m_s)}\rangle,$$
 (58)

with $\bar{x}_n^{(m_s)} = x_n^{(m_s)}/\sqrt{V_x^{(m_s)}}$ and $V_x^{(m_s)} = \sum_{n=0}^{2^{12}-1} |x_n^{(m_s)}|^2$. Note that $|n^{(m_s)}\rangle$ in Eq. (58) is the basis labeled by Eq. (1) within the m_s th segment. Therefore, each $|\Psi_c^{(m_s)}\rangle$ is properly normalized within the segment, i.e., $\langle \Psi_c^{(m_s)}|\Psi_c^{(m_s)}\rangle=1$. The quantum state $|\Psi_c^{(m_s)}\rangle$ in Eq. (58) is now expressed with a smaller number of qubits L=12 and each $|\Psi_c^{(m_s)}\rangle$ is encoded separately into a quantum circuit state $\hat{\mathcal{C}}^{(m_s)}|0\rangle$ using the AQCE algorithm, which is expected to be easier than the case for L=16. We should however note that the total Hilbert space defining $|\tilde{\Psi}_c\rangle$ in Eq. (57) is now increased to $2^{12\times 16}=2^{192}$ from 2^{16} for $|\Psi_c\rangle$ to represent the 2^{16} dimensional classical data, suggesting that the input classical data is mapped into a higher dimensional space via a feature map $|\tilde{\Psi}_c\rangle$ [10,18,19,73]. Although we do not perform any further explicit demonstration, this might find an interesting application of quantum machine learning based on a kernel method [10,18,19,73].

We employ the AQCE algorithm to encode separately the quantum state $|\Psi_c^{(m_s)}\rangle$ representing the m_s th segment of the picture with the control parameters $(M_0, N, \delta M) =$ (12, 100, 6) and varying the total number M of two-qubit unitary operators in the quantum circuit $\hat{C}^{(m_s)}$. Figures 11(g)– 11(i) show the reconstructed pictures by decoding the quantum circuit states $\hat{C}^{(m_s)}|0\rangle$ with properly rescaling back the amplitude $\bar{x}_n^{(m_s)'} = \langle n^{(m_s)}|\hat{C}^{(m_s)}|0\rangle$ by the m_s dependent volume $\sqrt{V_x^{(m_s)}}$. We find that the original picture is reconstructed very efficiently with a much less number M of two-qubit unitary operators, as compared with the results of encoding the whole picture without the segmentation shown in Figs. 11(c)–11(e). The fidelity between the quantum state $|\Psi_{c}^{(m_s)}\rangle$ representing the m_s th segment of the picture and the quantum circuit state $\hat{C}^{(m_s)}|0\rangle$ is also shown in Fig. 12. We observe that the fidelity can be improved much more efficiently with increasing M when the whole picture is divided into many pieces to decrease the dimension of the classical data that is to be encoded into a quantum circuit with a less number L of qubits.

Recall now that a 64×64 pixels picture is given by a $2^{12} = 4096$ dimensional vector. While an SU(4) operator (i.e., a two-qubit unitary operator with ignoring a global phase) is parametrized by 15 independent real parameters, two consecutive single-qubit Euler rotations are redundant (see Fig. 16). Removing these redundancies, the number of the independent real parameters for a quantum circuit with M number of SU(4) operators is 9M + 3L. Therefore, the number of the independent real parameters for the quantum circuit with M = 480 on L = 12 qubits is almost equal to the dimension of the segmented picture. As shown in Fig. 11(i), we indeed find that the reconstructed picture reproduces the original picture with a reasonable accuracy.

How is this quantum circuit encoding of classical data potentially useful in the context of quantum machine learning? To make good use of quantum computers for machine learning, classical data has to be implemented into a quantum device in the first place. As explained above, a quantum state representing classical data via, e.g., the amplitude encoding is generally too complicated to be prepared in a quantum device naively. The quantum circuit encoding proposed here can be employed for this purpose to approximately construct a quantum circuit representing a quantum state of classical data with controlled accuracy. This can be done on a classical computer and has been indeed recently applied in Ref. [74] using the AQCE algorithm proposed here. The obtained quantum circuit is then implemented in a quantum device for further processing of machine learning. In the next section, we shall demonstrate experimentally some of this procedure.

IV. EXPERIMENTAL DEMONSTRATION USING A QUANTUM DEVICE

Although the quantum-classical hybrid computation of the AQCE algorithm is in principle possible, we find that the implementation using currently available quantum devices is practically difficult. Therefore, here we instead experimentally demonstrate that the AQCE algorithm indeed generates a quantum circuit that can be implemented on a real quantum device to produce a desired quantum state with reasonable accuracy.

For this demonstration, we use a quantum device (ibmq lima) provided by IBM Quantum [49] with the Qiskit Python API for programming the device [75]. The processor type of ibmq_lima is Falcon r4T with its qubit topology shown in Fig. 13(a), and we used qubits labeled 0 and 1 for the two-qubit experiments and qubits labeled by 0, 1, and 2 for the three-qubit experiments. All experimental data were collected on 15 October 2021. The qubit frequencies ω , decoherence times T_1 and T_2 , readout errors ε_r , and state-preparation-and-measurement errors ε_s (probabilities measuring state $|0\rangle_i$ after preparing state $|1\rangle_i$, which were larger than probabilities measuring state $|1\rangle_i$ after preparing state $|0\rangle_i$) for qubits 0, 1, and 2 were $(\omega, T_1, T_2, \varepsilon_r, \varepsilon_s)$ $= (5.0297314 \text{ GHz}, 112.76330 \text{ }\mu\text{s}, 63.266823 \text{ }\mu\text{s}, 0.0266,$ 0.0438), (5.1276895 GHz, 107.94655 us, 127.49361 us, 0.0292, 0.0464), and (5.2473447 GHz, 116.56877 µs, 109.85284 µs, 0.0286, 0.0458), respectively. The controlled-

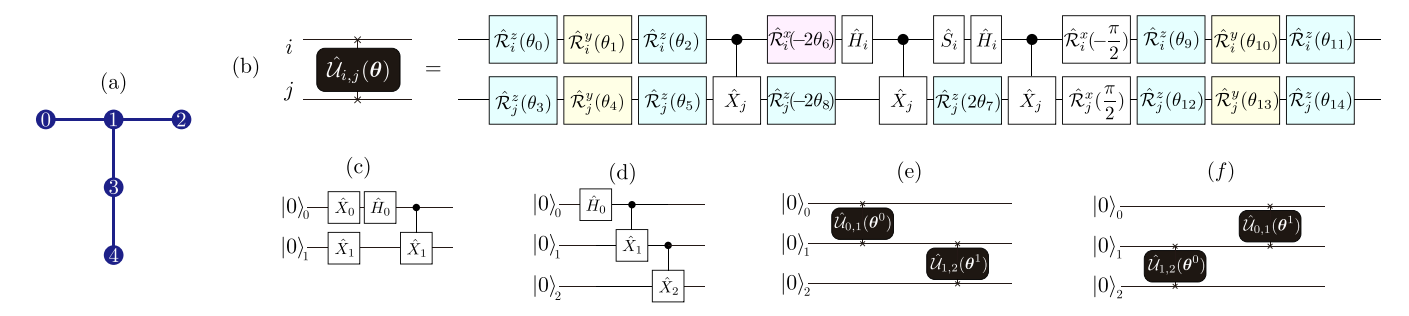


FIG. 13. (a) Qubit topology of ibmq_lima provided by IBM Quantum [49]. Numbers indicate labels of qubits and solid lines denote connectivity of qubits. (b) Two-qubit unitary operator $\hat{\mathcal{U}}_{i,j}(\boldsymbol{\theta})$ acting on qubit i and j is implemented on a quantum device by a standard set of quantum gates with 15 parameters $\boldsymbol{\theta} = \{\theta_0, \theta_1, \cdots, \theta_{14}\}$ for the rotation angles of single-qubit gates. (c) Quantum circuit $\hat{\mathcal{U}}_{\text{2QS}}$ that generates the singlet state $|\Psi_{\text{2QS}}\rangle$ in the two-qubit space. (d) Quantum circuit $\hat{\mathcal{U}}_{\text{GHZ}}$ that generates the GHZ state $|\Psi_{\text{GHZ}}\rangle$ in three-qubit space. (e), (f) Quantum circuit structures obtained by the AQCE algorithm for a quantum state in the three-qubit space, containing two two-qubit unitary operators acting on qubits that are physically connected in the quantum device employed here.

NOT error for qubits 0 and 1 was 0.0071634 and that for qubits 1 and 2 was 0.0070542. However, we have obtained essentially the same results on different dates and thus under the different calibration conditions.

A. Quantum states in the two-qubit space

We first consider one of the simplest quantum states, i.e., the singlet state in the two-qubit space (one of the Bell states) given by

$$|\Psi_{2QS}\rangle = \frac{1}{\sqrt{2}}(|01\rangle - |10\rangle),\tag{59}$$

where $|01\rangle = |0\rangle_0 \otimes |1\rangle_1$ and $|10\rangle = |1\rangle_0 \otimes |0\rangle_1$, following the notation introduced at the beginning of Sec. II A. We apply the AQCE algorithm on a classical computer to encode the quantum state $|\Psi_{2QS}\rangle$ and obtain within the machine precision that

$$|\Psi_{2OS}\rangle = \hat{\mathcal{U}}_{0.1}(\boldsymbol{\theta})|0\rangle, \tag{60}$$

where the quantum circuit $\hat{\mathcal{U}}_{i,j}(\boldsymbol{\theta})$ operating on qubits i and j is given as

$$\hat{\mathcal{U}}_{i,j}(\boldsymbol{\theta}) = \hat{\mathcal{R}}_{j}^{z}(\theta_{14})\hat{\mathcal{R}}_{j}^{y}(\theta_{13})\hat{\mathcal{R}}_{j}^{z}(\theta_{12})\hat{\mathcal{R}}_{i}^{z}(\theta_{11})\hat{\mathcal{R}}_{i}^{y}(\theta_{10})\hat{\mathcal{R}}_{i}^{z}(\theta_{9})
\times \hat{\mathcal{R}}_{j}^{x}(\pi/2)\hat{\mathcal{R}}_{i}^{x}(-\pi/2)\hat{C}_{i}(\hat{X}_{j})\hat{H}_{i}\hat{S}_{i}
\times \hat{\mathcal{R}}_{j}^{z}(2\theta_{7})\hat{C}_{i}(\hat{X}_{j})\hat{\mathcal{R}}_{j}^{z}(-2\theta_{8})\hat{H}_{i}\hat{\mathcal{R}}_{i}^{x}(-2\theta_{6})\hat{C}_{i}(\hat{X}_{j})
\times \hat{\mathcal{R}}_{j}^{z}(\theta_{5})\hat{\mathcal{R}}_{j}^{y}(\theta_{4})\hat{\mathcal{R}}_{j}^{z}(\theta_{3})\hat{\mathcal{R}}_{i}^{z}(\theta_{2})\hat{\mathcal{R}}_{i}^{y}(\theta_{1})\hat{\mathcal{R}}_{i}^{z}(\theta_{0}),$$
(6)

and the resulting set of parameters $\boldsymbol{\theta} = \{\theta_0, \theta_1, \cdots, \theta_{14}\}$ is displayed in Table I. Here, $\hat{\mathcal{R}}_i^z(\theta) = e^{-\mathrm{i}\theta\hat{\mathcal{L}}_i/2}$ represents a single-qubit rotation around the z axis at qubit i, with similar definitions for $\hat{\mathcal{R}}_i^x(\theta)$ and $\hat{\mathcal{R}}_i^y(\theta)$, and $\hat{\mathcal{C}}_i(\hat{X}_j)$ denotes the controlled-NOT (CNOT) gate where the NOT operation acting on the jth qubit is controlled by the ith qubit. The explicit form of the quantum circuit $\hat{\mathcal{U}}_{i,j}(\boldsymbol{\theta})$ and the associated quantum gates are shown in Fig. 13(b). Note that the singlet state in Eq. (59) can also be prepared simply by

$$|\Psi_{2QS}\rangle = \hat{\mathcal{U}}_{2QS}|0\rangle, \tag{62}$$

with the quantum circuit

$$\hat{\mathcal{U}}_{2OS} = \hat{C}_0(\hat{X}_1)\hat{H}_0\hat{X}_1\hat{X}_0, \tag{63}$$

as shown in Fig. 13(c).

By using the quantum device, we evaluate in Figs. 14(a) and 14(b) the density matrix, $[\rho]_{nn'} = \langle n|\hat{\rho}|n'\rangle$, of the singlet state generated by the quantum circuits \hat{U}_{2QS} in Eq. (63) and $\hat{U}_{0,1}(\theta)$ in Eq. (61), respectively. Here, $|n\rangle$ and $|n'\rangle$ with n, n' = 0, 1, 2, 3 are the basis states of L = 2 qubits labeled as in Eq. (1). To evaluate the density matrix, we perform the quantum state tomography by measuring 16 different sets of Pauli strings (including the identity operator) with length two [see Eqs. (42) and (43)]. Each Pauli string is measured on the quantum device 4096 times and the density matrix $[\rho]_{nn'}$ shown in Figs. 14(a) and 14(b) is evaluated from the averaged values over these measurements. These results are also compared with the exact values. We find that the density matrices evaluated on the quantum device with the two different quantum circuits, one obtained by the AQCE algorithm,

TABLE I. Sets of parameters $\boldsymbol{\theta} = \{\theta_0, \theta_1, \cdots, \theta_{14}\}$ for the quantum circuits $\hat{\mathcal{U}}_{0,1}(\boldsymbol{\theta})$ in Eq. (61) [also see Fig. 13(b)] generated by the AQCE algorithm, encoding the singlet state $|\Psi_{2QS}\rangle$ and the random state $|\Psi_{2QS}\rangle$ in the two-qubit space.

	Singlet state	Random state
$\overline{\theta_0}$	1.6823068	2.0216448
θ_1	3.1415927	1.3683389
θ_2	0	-2.2863607
θ_3	-0.9758576	-2.8429004
θ_4	0	1.9027058
θ_5	-1.6678105	-1.8420845
θ_6	0.3926991	0.7086172
θ_7	3.5342917	1.1534484
θ_8	3.1355175	1.6383263
θ_9	-2.6094912	-2.6132016
θ_{10}	-3.1415927	-2.0676228
θ_{11}	3.1204519	2.1424122
θ_{12}	-1.6869951	-1.2293439
θ_{13}	-3.1415926	-1.8418481
θ_{14}	2.4721516	-2.6729236

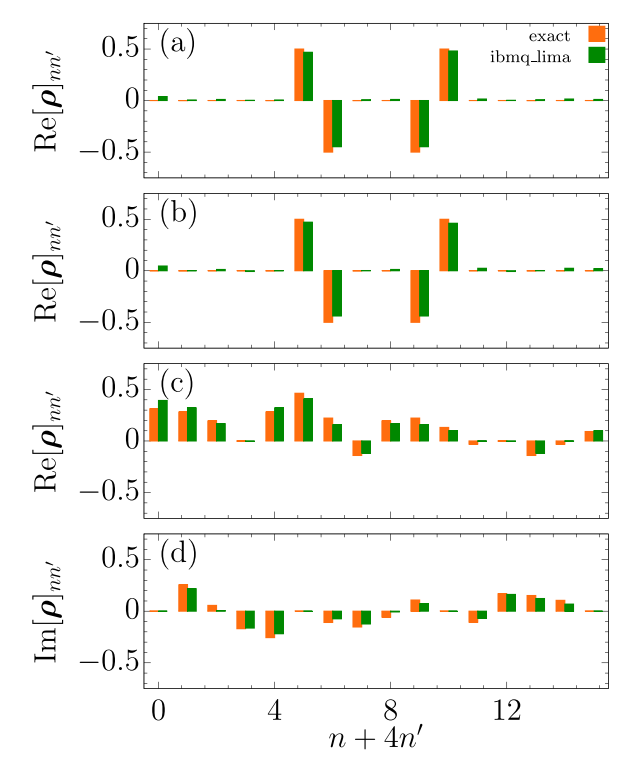


FIG. 14. (a) Density matrix $[\rho]_{nn'} = \langle n|\hat{\rho}|n'\rangle$ evaluated on the quantum device (ibmq_lima) with the quantum circuit $\hat{\mathcal{U}}_{2OS}$ describing the singlet state $|\Psi_{2OS}\rangle$ in Eq. (59). (b) Same as panel (a) but with the quantum circuit $\hat{\mathcal{U}}_{0,1}(\boldsymbol{\theta})$ in Eq. (61) generated by the AQCE algorithm encoding the singlet state $|\Psi_{2OS}\rangle$. The parameter set θ is provided in the column "singlet state" of Table I. Note that only the real part of density matrix is shown in panels (a) and (b) because the imaginary part is zero for the singlet state $|\Psi_{2OS}\rangle$. (c) Real and (d) imaginary parts of density matrix $[\rho]_{nn'} = \langle n|\hat{\rho}|n'\rangle$ evaluated on the quantum device (ibmq_lima) with the quantum circuit $\hat{\mathcal{U}}_{0,1}(\boldsymbol{\theta})$ in Eq. (61) generated by the AQCE algorithm encoding the random state $|\Psi_{2QR}\rangle$ in Eq. (65) [also see Eq. (C1)]. The parameter set θ is provided in the column "random state" of Table I. For comparison, the exact results are also shown by orange bars. The density matrix is evaluated on the quantum device by the quantum state tomography, measuring 16 different sets of Pauli strings with length two, and the results shown here are obtained from the averaged values over 4096 measurements of each Pauli string. $|n\rangle$ and $|n'\rangle$ with n, n' = 0, 1, 2, 3are the basis states of L=2 qubits labeled as in Eq. (1).

are rather similar and can both reproduce the exact result with reasonable accuracy.

For quantitative comparison, we now introduce the following quantity:

$$Q = (\operatorname{Tr}[\hat{\rho}_A \hat{\rho}_B])^{1/2}, \tag{64}$$

where $\hat{\rho}_A$ and $\hat{\rho}_B$ are the density operators of two quantum states A and B. Here we employ this quantity as fidelity of two quantum states because some of the eigenvalues of the density matrix evaluated from our experimental measurements are negative. This can be justified when two quantum states A and B are pure states, i.e., $\hat{\rho}_A = |\Psi_A\rangle\langle\Psi_A|$ and $|\Psi_B\rangle\langle\Psi_B|$, because in this case $Q = |\langle\Psi_A|\Psi_B\rangle|$. Using the density matrix evaluated experimentally in Fig. 14(b), we find that the fidelity Q for the exact singlet state $|\Psi_{2QS}\rangle$ and the singlet state

generated by the quantum circuit $\hat{\mathcal{U}}_{0,1}(\boldsymbol{\theta})$ is as large as 0.9512. This is indeed comparable to the fidelity Q=0.9607 for the exact singlet state $|\Psi_{2QS}\rangle$ and the singlet state generated by the quantum circuit $\hat{\mathcal{U}}_{2QS}$.

Next, we consider the case where a quantum state is more complex in the sense that the associated density matrix has many nonzero elements. To this end, we examine a random state described by the following state in the two-qubit space:

$$|\Psi_{2QR}\rangle = \sum_{\sigma_0 = 0, 1} \sum_{\sigma_1 = 0, 1} \psi_{\sigma_0 \sigma_1}^{\mathrm{r}} |\sigma_0 \sigma_1\rangle, \tag{65}$$

where $|\sigma_0\sigma_1\rangle = |\sigma_0\rangle_0 \otimes |\sigma_1\rangle_1$. The coefficients $\psi^{\rm r}_{\sigma_0\sigma_1}$ are randomly determined as follows: We first use a random generator in the c + + standard library for the normal distribution with the mean 0 and the standard deviation 1 to determine the real and imaginary parts of each coefficient and then normalize the resulting state [76]. The values of coefficients $\psi_{\sigma_0\sigma_1}^{\rm r}$ used in the demonstration can be found in Appendix C. We apply the AQCE algorithm on a classical computer to encode the quantum state $|\Psi_{2QR}\rangle$ and obtain the quantum circuit $\hat{\mathcal{U}}_{0,1}(\boldsymbol{\theta})$ with the parameter set $\theta = \{\theta_1, \theta_2, \dots, \theta_{14}\}$ given in Table I, which can represent $|\Psi_{2OR}\rangle$ exactly within the machine precision. The density matrix $[\rho]_{nn'}$ of the random state generated by the quantum circuits $\hat{\mathcal{U}}_{0,1}(\boldsymbol{\theta})$ is evaluated on the quantum device in Figs. 14(c) and 14(d) by using the quantum state tomography described above. Similar to the case of the singlet state, we find that the results evaluated on the quantum device are rather well compared with the exact values. Indeed, using the density matrix evaluated experimentally in Figs. 14(c) and 14(d), we find that the fidelity Q for the exact random state $|\Psi_{2QR}\rangle$ and the random state generated by the quantum circuit $\hat{\mathcal{U}}_{0,1}(\boldsymbol{\theta})$ is as large as 0.9592.

B. Quantum states in the three-qubit space

The demonstrations shown above are focused on quantum states in the two-qubit space. It is also highly interesting to continue a similar demonstration for a quantum state in a larger Hilbert space. Let us now consider the GHZ state in the three-qubit space given by

$$|\Psi_{\text{GHZ}}\rangle = \frac{1}{\sqrt{2}}(|000\rangle + |111\rangle),\tag{66}$$

where $|000\rangle = |0\rangle_0 \otimes |0\rangle_1 \otimes |0\rangle_2$ and $|111\rangle = |1\rangle_0 \otimes |1\rangle_1 \otimes |1\rangle_2$, following the notation introduced at the beginning of Sec. II A. It is known that the GHZ state can be prepared simply by

$$|\Psi_{\text{GHZ}}\rangle = \hat{\mathcal{U}}_{\text{GHZ}}|0\rangle,\tag{67}$$

with the quantum circuit

$$\hat{\mathcal{U}}_{GHZ} = \hat{C}_1(\hat{X}_2)\hat{C}_0(\hat{X}_1)\hat{H}_0 \tag{68}$$

acting on qubits 0, 1, and 2, as shown in Fig. 13(d).

We also perform the AQCE algorithm on a classical computer to encode the GHZ state into a quantum circuit. Considering a set of bonds \mathbb{B} in the AQCE algorithm, it is wise to include only pairs of qubits that are physically connected in the quantum device to decrease the number of extra quantum gates. In the quantum device employed in this demonstration,

TABLE II. Sets of parameters $\boldsymbol{\theta}^m = \{\theta_0^m, \theta_1^m, \cdots, \theta_{14}^m\}$ (m=0 and 1) for the quantum circuit $\hat{\mathcal{U}}_{0,1,2}(\boldsymbol{\theta})$ in Eq. (70) [also see Fig. 13(e)] generated by the AQCE algorithm, encoding the GHZ state $|\Psi_{\text{GHZ}}\rangle$ in the three-qubit space.

	m = 0	m = 1
θ_0^m	0.70081942	0
θ_1^m	1.59343588	0
θ_2^m	-2.99819974	0
θ_3^m	3.01209222	0.03670498
θ_4^m	1.45398911	1.57079633
θ_5^m	-2.86368415	0
θ_6^m	0.25868788	0.25573854
θ_6^m θ_7^m	0.14505637	0
θ_8^m	-0.63764672	-2.35619449
θ_9^m	-1.71718177	0
θ_{10}^m	-2.80049545	-3.14159265
θ_{11}^m	-2.60125707	0.04066063
θ_{12}^m	-2.13304918	-1.57079633
θ_{13}^m	1.68590984	-1.57079633
θ_{14}^m	-2.04727870	-1.11421776

there are only two pairs of qubits: $\mathbb{B} = \{\{0, 1\}, \{1, 2\}\}$. However, it is not obvious in advance how many two-qubit unitary operators $\hat{\mathcal{U}}_{i,j}(\boldsymbol{\theta})$ are necessary to encode the GHZ state. By performing the AQCE algorithm on a classical computer, we find within the machine precision that

$$|\Psi_{\text{GHZ}}\rangle = \hat{\mathcal{U}}_{0,1,2}(\boldsymbol{\theta})|0\rangle, \tag{69}$$

with the quantum circuit $\hat{\mathcal{U}}_{0,1,2}(\theta)$ being composed of two two-qubit unitary operators,

$$\hat{\mathcal{U}}_{0,1,2}(\boldsymbol{\theta}) = \hat{\mathcal{U}}_{1,2}(\boldsymbol{\theta}^1)\hat{\mathcal{U}}_{0,1}(\boldsymbol{\theta}^0), \tag{70}$$

where $\theta = \{\theta^0, \theta^1\}$ and the resulting sets of parameters $\theta^m = \{\theta_0^m, \theta_1^m, \cdots, \theta_{14}^m\}$ (m = 0 and 1) for $\hat{\mathcal{U}}_{0,1}(\theta^0)$ and $\hat{\mathcal{U}}_{1,2}(\theta^1)$ are provided in Table II with $\hat{\mathcal{U}}_{i,j}(\theta)$ being defined in Eq. (61) and Fig. 13(b). The schematic structure of the quantum circuit is shown in Fig. 13(e). Notice in Table II that $\theta_0^1 = \theta_1^1 = \theta_2^1 = 0$ because these parameters correspond to the first Euler rotation (acting on qubit 1) of the second two-qubit unitary operator $\hat{\mathcal{U}}_{1,2}(\theta^1)$, which can be absorbed into the last Euler rotation of the first two-qubit unitary operator $\hat{\mathcal{U}}_{0,1}(\theta^1)$. We should also note that since the GHZ state is translational symmetric, the quantum circuit with the structure shown in Fig. 13(f) is topologically equivalent. The AQCE algorithm select one of them and, in this particular demonstration, the quantum circuit with the structure shown in Fig. 13(e) is selected.

Next, using the quantum device, we evaluate in Figs. 15(a) and 15(b) the density matrix, $[\rho]_{nn'} = \langle n|\hat{\rho}|n'\rangle$, of the GHZ state generated by the quantum circuits $\hat{\mathcal{U}}_{GHZ}$ in Eq. (68) and $\hat{\mathcal{U}}_{0,1,2}(\theta)$ in Eq. (70), respectively. Here, $|n\rangle$ and $|n'\rangle$ with $n, n' = 0, 1, 2, \ldots, 7$ are the basis states of L = 3 qubits labeled as in Eq. (1). Similar to the cases of L = 2 qubits discussed in Sec. IV A, we evaluate the density matrix by performing the quantum state tomography, where 64 different sets of Pauli strings (including the identity operator) with length three [see Eqs. (42) and (43) for L = 2 qubits] are measured. The density matrix $[\rho]_{nn'}$ shown in Figs. 15(a) and 15(b) is evaluated from the averaged values of Pauli strings

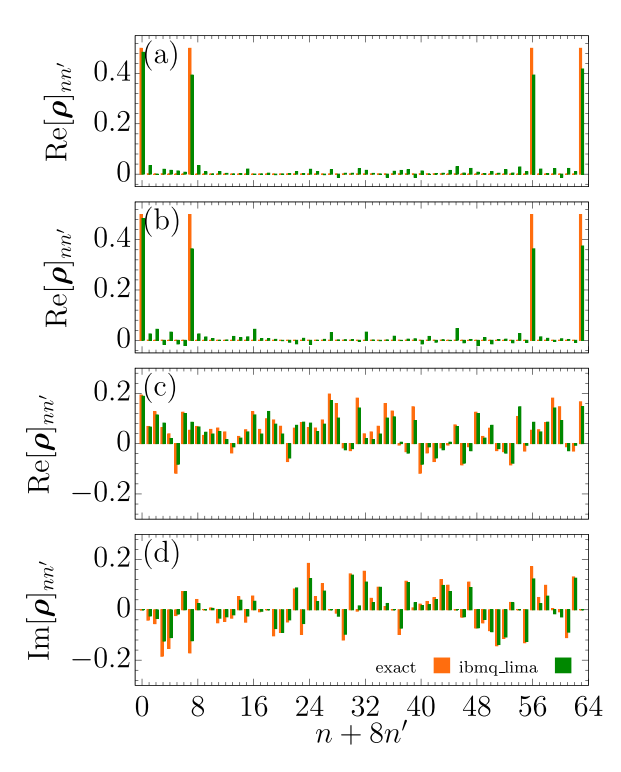


FIG. 15. (a) Density matrix $[\rho]_{nn'} = \langle n | \hat{\rho} | n' \rangle$ evaluated on the quantum device (ibmq_lima) with the quantum circuit $\hat{\mathcal{U}}_{GHZ}$ describing the GHZ state $|\Psi_{GHZ}\rangle$ in Eq. (66). (b) Same as panel (a) but with the quantum circuit $\hat{\mathcal{U}}_{0,1,2}(\boldsymbol{\theta})$ in Eq. (70) generated by the AQCE algorithm encoding the GHZ state $|\Psi_{GHZ}\rangle$. The parameter set θ is provided in Table II. Note that only the real part of density matrix is shown in panels (a) and (b) because the imaginary part is zero for the GHZ state $|\Psi_{GHZ}\rangle$. (c) Real and (d) imaginary parts of density matrix $[\rho]_{nn'} = \langle n|\hat{\rho}|n'\rangle$ evaluated on the quantum device (ibmq_lima) with the quantum circuit $\hat{\mathcal{U}}'_{0,1,2}(\theta)$ in Eq. (73) generated by the AQCE algorithm encoding the random state $|\Psi_{3QR}\rangle$ in Eq. (71) [also see Eq. (C2)]. The parameter set θ is provided in Table III. For comparison, the exact results are also shown by orange bars. The density matrix is evaluated on the quantum device by the quantum state tomography, measuring 64 different sets of Pauli strings with length three, and the results shown here are obtained from the averaged values over 4096 measurements of each Pauli string. $|n\rangle$ and $|n'\rangle$ with $n, n' = 0, 1, 2, \dots, 7$ are the basis states of L = 3 qubits labeled as in Eq. (1).

measured 4096 times each. Although the number of quantum gates in the quantum circuit $\hat{\mathcal{U}}_{0,1,2}(\theta)$ is much larger than that in the quantum circuit $\hat{\mathcal{U}}_{GHZ}$, we find that the density matrices evaluated on the quantum device with these two different quantum circuits are rather similar and are in reasonable agreement with the exact values. More quantitatively, using the density matrix evaluated experimentally in Fig. 15(b), we find that the fidelity Q for the exact GHZ state $|\Psi_{GHZ}\rangle$ and the GHZ state generated by the quantum circuit $\hat{\mathcal{U}}_{0,1,2}(\theta)$ is as large as 0.8906. This is comparable to the fidelity Q=0.9189 for the exact GHZ state $|\Psi_{GHZ}\rangle$ and the GHZ state generated by the quantum circuit $\hat{\mathcal{U}}_{GHZ}$.

Finally, we examine a random state in the three-qubit space:

$$|\Psi_{3QR}\rangle = \sum_{\sigma_0=0,1} \sum_{\sigma_1=0,1} \sum_{\sigma_2=0,1} \psi_{\sigma_0\sigma_1\sigma_2}^{r} |\sigma_0\sigma_1\sigma_2\rangle, \quad (71)$$

TABLE III. Sets of parameters $\boldsymbol{\theta}^m = \{\theta_0^m, \theta_1^m, \cdots, \theta_{14}^m\}$ (m=0 and 1) for the quantum circuit $\hat{\mathcal{U}}'_{0,1,2}(\boldsymbol{\theta})$ in Eq. (73) [also see Fig. 13(f)] generated by the AQCE algorithm, encoding the random state $|\Psi_{3QR}\rangle$ in the three-qubit space.

	m = 0	m = 1
θ_0^m	1.39099869	0.12699636
θ_1^m	1.22253363	1.49657252
θ_2^m	-1.22510250	-0.96112628
θ_3^m	-1.04474694	0
θ_4^m	1.85347535	0
θ_5^m	-2.24417198	0
θ_6^m	-1.06037512	-0.39222573
θ_7^m	-0.87968547	0.60984155
θ_8^m	-0.05457889	-0.07696758
θ_9^m	0.03359139	0.48406694
θ_{10}^m	2.27862931	-0.36703453
θ_{11}^m	0.49867804	0.19553219
θ_{12}^m	2.89140237	-1.17312888
θ_{13}^m	-0.80188802	-2.29176295
θ_{14}^m	1.52534544	-3.06220240

where $|\sigma_0\sigma_1\sigma_2\rangle = |\sigma_0\rangle_0 \otimes |\sigma_1\rangle_1 \otimes |\sigma_2\rangle_2$, and the coefficients are randomly determined as in the case of the random state $|\Psi_{2QR}\rangle$ in Eq. (65). The values of coefficients $\psi^r_{\sigma_0\sigma_1\sigma_2}$ used in the demonstration can be found in Appendix C. We perform the AQCE algorithm on a classical computer and obtain within the machine precision that

$$|\Psi_{3OR}\rangle = \hat{\mathcal{U}}_{0,1,2}'(\boldsymbol{\theta})|0\rangle, \tag{72}$$

with the quantum circuit

$$\hat{\mathcal{U}}'_{0,1,2}(\theta) = \hat{\mathcal{U}}_{0,1}(\theta^1)\hat{\mathcal{U}}_{1,2}(\theta^0), \tag{73}$$

where $\boldsymbol{\theta} = \{\boldsymbol{\theta}^0, \boldsymbol{\theta}^1\}$ and the resulting sets of parameters $\boldsymbol{\theta}^m = \{\theta_0^m, \theta_1^m, \cdots, \theta_{14}^m\}$ (m=0 and 1) for $\hat{\mathcal{U}}_{1,2}(\boldsymbol{\theta}^0)$ and $\hat{\mathcal{U}}_{0,1}(\boldsymbol{\theta}^1)$ are provided in Table III with $\hat{\mathcal{U}}_{i,j}(\boldsymbol{\theta})$ being defined in Eq. (61) and Fig. 13(b). The schematic structure of the quantum circuit $\hat{\mathcal{U}}'_{0,1,2}(\boldsymbol{\theta})$ is shown in Fig. 13(f). Here, we should note that, depending of the initialization process, the AQCE algorithm also finds a quantum circuit forming the structure shown in Fig. 13(e) with a different set of parameters $\boldsymbol{\theta}$, which can encode the random state $|\Psi_{3QR}\rangle$ exactly within the machine precision. This implies that two two-qubit unitary operators are enough to encode any quantum state in the three-qubit space.

We perform the quantum state tomography on the quantum device to evaluate the density matrix $[\rho]_{nn'}$ of the random state generated by the quantum circuit $\hat{\mathcal{U}}'_{0,1,2}(\theta)$. The 64 different Pauli strings with length three are measured 4096 times each and the density matrix shown in Figs. 15(c) and 15(d) is obtained from the averaged values of these measurements. Using the density matrix evaluated experimentally in Figs. 15(c) and 15(d), we find that the fidelity Q for the exact random state $|\Psi_{3QR}\rangle$ and the random state generated by the quantum circuit $\hat{\mathcal{U}}'_{0,1,2}(\theta)$ is as large as 0.9051, suggesting good accordance with the exact result.

V. SUMMARY

We have proposed the quantum circuit encoding algorithm to encode a given quantum state $|\Psi\rangle$ onto a quantum circuit $\hat{\mathcal{C}}$ composed of K-qubit unitary operators $\{\hat{\mathcal{U}}_m\}$ by maximizing the absolute value of the fidelity $F = \langle 0|\hat{\mathcal{C}}^{\dagger}|\Psi\rangle$. The fidelity |F| can be maximized by sequentially optimizing each unitary operator $\hat{\mathcal{U}}_m$ one by one via SVD of the fidelity tensor matrix F_m , a similar scheme used for the optimization in the tensor network method. The most demanding part of the algorithm is to construct the fidelity tensor matrix F_m and we have shown how a quantum computer can be utilized for this task. The AQCE algorithm proposed here determines not only the form of the individual unitary operators but also the optimal location of qubits on which each unitary operator acts in the quantum circuit. Therefore, it allows us to generate an optimal quantum circuit of a given quantum state automatically. The elementary single- and two-qubit gates are algebraically assigned when the encoded quantum circuit is composed of two-qubit unitary operators. We emphasize that the AQCE algorithm proposed here does not rely on any parametrized quantum circuit as in variational quantum algorithms such as VQE and thus the associated parameter optimization is not required.

Using numerical simulations, we have demonstrated the AQCE algorithm to encode a ground state of a quantum manybody system, such as the spin-1/2 isotropic antiferromagnetic Heisenberg model and the spin-1/2 XY model in one spatial dimension, onto a quantum circuit composed of two-qubit unitary operators. We have also compared the results with the quantum circuit encoding of the same quantum state onto a quantum circuit in a given circuit structure such as the Trotter-like and MERA-like circuit structures and found that the quantum circuit generated by the AQCE algorithm is better than the Trotter-like circuit and is equally competitive with the MERA-like circuit.

We have also demonstrated that the AQCE algorithm can be applied to encode a quantum state representing classical data such as a classical image. As a concrete example, we considered a gray scale picture of 256×256 pixels, which can be expressed as a quantum state $|\Psi_c\rangle$ on 16 qubits by using the amplitude encoding, and thus can be encoded onto a quantum circuit \hat{C} by employing the AQCE algorithm. Although the picture reconstructed by decoding the quantum circuit state $\hat{C}|0\rangle$ improves its quality systematically with increasing the number of two-qubit unitary operators in the quantum circuit \hat{C} , the improvement is relatively slow if the size of the picture is large. Therefore, we have also made a different attempt by dividing the original picture into 16 pieces, which thus allows us to represent each segment of the picture of 64 × 64 pixels with a quantum state $|\Psi_c^{(m_s)}\rangle$ on 12 qubits for $m_s = 1, 2, ..., 16$. This implies that the original classical data is represented by a direct product of 16 quantum states $|\Psi_c^{(m_s)}\rangle$, which is thus defined in a higher dimensional space than the input classical data. We have encoded each quantum state $|\Psi_c^{(m_s)}\rangle$ separately onto a different quantum circuit $\hat{C}^{(m_s)}$ and found that the quality of the reconstructed picture by decoding all these quantum circuit states $\hat{C}^{(m_s)}|0\rangle$ is much improved. This is encouraging for a near-term application because, depending on available quantum devices, one can adjust the number of qubits by dividing classical data into multiple pieces. In the context of quantum machine learning, the AQCE algorithm would be potentially useful for finding an optimal quantum circuit, which can be done classically, to prepare a quantum state representing classical data that is to be processed on a quantum computer for machine learning.

Moreover, we have used the quantum device provided by IBM Quantum to demonstrate experimentally that quantum circuits generated by the AQCE algorithm can be implemented on a real quantum device to produce a desired quantum state with reasonable accuracy. For this purpose, we have considered the well-known quantum states, such as the singlet state and the GHZ state, as well as random states in the two- and three-qubit spaces, and shown that the density matrix evaluated on the quantum device for the quantum circuits obtained by the AQCE algorithm is indeed compatible with the exact values.

As clearly demonstrated for several examples, the AQCE algorithm can encode a given quantum state onto a quantum circuit with controlled accuracy by varying the number M of unitary operators $\{\hat{\mathcal{U}}_m\}$ in the quantum circuit. One of the advantages of the AQCE algorithm is that it requires very little adjustable parameters, regardless of the problem. For example, the VQE algorithm requires many adjustable parameters to be set such as circuit ansatz and learning rate, but the AQCE algorithm requires only the number of iterations. However, we have observed that the improvement of accuracy with increasing M becomes sometimes slower when the number of qubits is large. For example, the results for 16 qubits show the accuracy of the fidelity per site, 1 - |F|, as good as 0.003, but it is expected that the optimization will become more difficult for larger system sizes.

There are two possible ways to further improve the AQCE algorithm. One is to improve the procedure of increasing the number of unitary operators by δM in the enlargement step of the algorithm (see Fig. 3). The procedure adopted as a prototype algorithm in this paper is to simply insert δM new unitary operators at the end of the quantum circuit. We have found that this simple strategy is not the most efficient. Instead, one may as well insert these new unitary operators in any location among already existing unitary operators. However, this is certainly more costly if a brute-force search is used.

Another way to improve the AQCE algorithm is related to how to generate and update unitary operators in the quantum circuit. In all the demonstrations, a quantum state is encoded directly onto a quantum circuit composed of unitary operators acting only on two qubits. However, as described in Secs. II, the space on which unitary operators act is not necessary the two-qubit space but the AQCE algorithm can encode a quantum state more generally onto a quantum circuit composed of K-qubit unitary operators with K > 2. One possible strategy is to encode a quantum state first onto a quantum circuit composed of unitary operators acting on a large qubit space, and these unitary operators are then decomposed into unitary operators acting on a smaller qubit space. We have found that this procedure can improve the accuracy significantly when the number of qubits is large and more details will be reported elsewhere.

ACKNOWLEDGMENTS

The authors are grateful to Kazuhiro Seki and Yuichi Otsuka for fruitful discussion. The calculation has been performed on the RIKEN supercomputer system (HOKU-SAI GreatWave) and the supercomputer Fugaku installed in RIKEN R-CCS through the HPCI system Research Project (Grants No. hp220217, No. hp230293, and No. hp230207). This work is supported by Grant-in-Aid for Scientific Research (A) (Grant No. 21H04446), Grant-in-Aid for Scientific Research (B) (Grants No. JP21H03455 and No. JP22H01171) and Grant-in-Aid for Scientific Research (C) (Grant No. JP22K03479) from MEXT, Japan, and Grant-in-Aid for Transformative Research Areas "The Natural Laws of Extreme Universe—A New Paradigm for Spacetime and Matter from Quantum Information" (Grants No. JP21H05182 and No. JP21H05191) from JSPS, Japan. It is also supported by JST PRESTO (Grant No. JPMJPR1911), MEXT Q-LEAP (Grant No. JPMXS0120319794), and JST COI-NEXT (Grants No. JPMJPF2014 and No. JPMJPF2221). It is also partially supported by Program for Promoting Research on the Supercomputer Fugaku (Grant No. JPMXP1020230411) form MEXT, Japan, by the New Energy and Industrial Technology Development Organization (NEDO) (Grant No. JPNP20017), and by the COE research grant in computational science from Hyogo Prefecture and Kobe City through Foundation for Computational Science. Additionally, we acknowledge the support from the UTokyo Quantum Initiative and the RIKEN TRIP initiative (RIKEN Quantum).

APPENDIX A: DECOMPOSITION OF A GENERAL TWO-QUBIT UNITARY OPERATOR

1. Decomposing into elementary quantum gates

In this Appendix, we briefly outline a procedure to decompose an arbitrary two-qubit unitary gate into elementary quantum gates [53]. As proven in Ref. [53], any two-qubit unitary operator \hat{U} acting on qubits i and j can be decomposed into a product of elementary gate operations in the following canonical form [also see Fig. 16(a)]:

$$\hat{\mathcal{U}} = e^{-i\alpha_0} \hat{\mathcal{R}}_i' \hat{\mathcal{R}}_j' \hat{\mathcal{D}} \hat{\mathcal{R}}_i \hat{\mathcal{R}}_j, \tag{A1}$$

where α_0 is an overall phase factor, not relevant for the assignment, $\hat{\mathcal{R}}_q'$ and $\hat{\mathcal{R}}_q$ are single-qubit Euler rotations acting on qubit q (= i, j) given by

$$\hat{\mathcal{R}}_q = e^{-i\xi_1^q \hat{Z}_q/2} e^{-i\xi_2^q \hat{Y}_q/2} e^{-i\xi_3^q \hat{Z}_q/2}$$
 (A2)

and

$$\hat{\mathcal{R}}'_{q} = e^{-i\zeta_{1}^{q}\hat{\mathcal{Z}}_{q}/2} e^{-i\zeta_{2}^{q}\hat{\mathcal{Y}}_{q}/2} e^{-i\zeta_{3}^{q}\hat{\mathcal{Z}}_{q}/2}, \tag{A3}$$

and $\hat{\mathcal{D}}$ is a two-qubit entangled operator

$$\hat{\mathcal{D}} = e^{-i(\alpha_1 \hat{X}_i \hat{X}_j + \alpha_2 \hat{Y}_i \hat{Y}_j + \alpha_3 \hat{Z}_i \hat{Z}_j)}.$$
 (A4)

By following the proof of Eq. (A1) in Ref. [53], the parameters ξ_k^q (k=1,2,3,q=i,j) and ζ_k^q (k=1,2,3,q=i,j) for the Euler rotations and α_k (k=1,2,3) for $\hat{\mathcal{D}}$ as well as α_0 are determined algebraically. For completeness, the derivation of Eq. (A1) is also provided in Appendix A 2. The total number

(a)
$$i \underbrace{\hat{\mathcal{L}}}_{j} = i \underbrace{\hat{\mathcal{R}}_{i}}_{j} \underbrace{\hat{\mathcal{R}}'_{i}}_{\hat{\mathcal{L}}} \underbrace{\hat{\mathcal{R}}'_{i}}_{\hat{\mathcal{L}}}$$

(b)
$$i \xrightarrow{\hat{\mathcal{D}}} = i \xrightarrow{\hat{u}_i^2} \hat{u}_i^3 \xrightarrow{\hat{w}_i} \hat{w}_i$$
$$j \xrightarrow{\hat{\mathcal{D}}} = j \xrightarrow{\hat{v}_j^2} \hat{v}_j^3 \xrightarrow{\hat{w}_j^3} \hat{w}_j^3$$

(c)
$$i \xrightarrow{\hat{\mathcal{U}}} = i \xrightarrow{\hat{u}_i^1} \hat{u}_i^2 \xrightarrow{\hat{u}_i^3} \hat{u}_i^4 \xrightarrow{\hat{u}_i^4} \hat{u}_i^4 \xrightarrow{\hat{u}_$$

FIG. 16. General form of a two-qubit unitary gate acting on qubits i and j. (a) Any unitary operator $\hat{\mathcal{U}}$ is decomposed into four single-qubit Euler rotations and two-qubit operator $\hat{\mathcal{D}}$. (b) $\hat{\mathcal{D}}$ is further decomposed into a product of the most standard quantum gates, including three controlled-NOT gates. (c) Decomposition of a unitary operator $\hat{\mathcal{U}}$ into a standard set of the most elementary quantum gates. Each single-qubit operation is defined in the text.

of parameters in the right hand side of Eq. (A1) is 16 and is identical to the number of free real parameters in a general U(4) matrix.

Next, as shown in Fig. 16(b), \hat{D} can be represented by a product of the most standard quantum gates [77,78]

$$\hat{\mathcal{D}} = \hat{w}_i \hat{w}_i^{\dagger} \hat{C}_i(\hat{X}_j) \hat{u}_i^3 \hat{v}_i^3 \hat{C}_i(\hat{X}_j) \hat{u}_i^2 \hat{v}_i^2 \hat{C}_i(\hat{X}_j). \tag{A5}$$

Here, $\hat{C}_i(\hat{X}_j)$ denotes the controlled-NOT gate defined previously in Eq. (61), and other gates are single qubit gates given by

$$\hat{w}_i = e^{i\pi \hat{X}_i/4}, \quad \hat{w}_i^{\dagger} = e^{-i\pi \hat{X}_j/4},$$
 (A6)

$$\hat{u}_i^3 = \hat{H}_i \hat{S}_i, \quad \hat{v}_i^3 = e^{-i\alpha_2 \hat{Z}_j}, \tag{A7}$$

$$\hat{u}_i^2 = \hat{H}_i e^{i\alpha_1 \hat{X}_i}, \quad \hat{v}_i^2 = e^{i\alpha_3 \hat{Z}_j}, \tag{A8}$$

with \hat{H}_i and \hat{S}_i being the Hadamard and shift gates, respectively. The matrix representations \boldsymbol{H} and \boldsymbol{S} for these quantum gates \hat{H}_i and \hat{S}_i in the computational basis are given, respectively, by

$$\boldsymbol{H} = \frac{1}{\sqrt{2}} \begin{pmatrix} 1 & 1 \\ 1 & -1 \end{pmatrix}, \quad \boldsymbol{S} = \begin{pmatrix} 1 & 0 \\ 0 & i \end{pmatrix}. \tag{A9}$$

Inserting the expression of Eq. (A5) into Eq. (A1), we obtain that

$$\hat{\mathcal{U}} = \hat{u}_i^4 \hat{v}_j^4 \hat{C}_i(\hat{X}_j) \hat{u}_i^3 \hat{v}_j^3 \hat{C}_i(\hat{X}_j) \hat{u}_i^2 \hat{v}_j^2 \hat{C}_i(\hat{X}_j) \hat{u}_i^1 \hat{v}_j^1, \tag{A10}$$

where

$$\hat{u}_i^1 = \hat{\mathcal{R}}_i, \quad \hat{v}_j^1 = \hat{\mathcal{R}}_j, \tag{A11}$$

$$\hat{u}_i^4 = \hat{\mathcal{R}}_i' \hat{w}_i, \quad \hat{v}_j^4 = \hat{\mathcal{R}}_j' \hat{w}_j^{\dagger}. \tag{A12}$$

This is also schematically shown in Fig. 16(c). Note that once the matrix representation for a single-qubit unitary operator is obtained, we can reparametrize any sequential product of single-qubit operators by using an overall phase factor and a

single Euler rotation algebraically (see Appendix B), suggesting that all \hat{u}_i^k (k=1,2,3,4) and \hat{v}_j^k (k=1,2,3,4) can be represented as single Euler rotations (apart from an overall phase factor). We should also note that when a matrix representation U of a unitary operator $\hat{\mathcal{U}}$ happens to be O(4), instead of U(4), the corresponding two-qubit operator for $\hat{\mathcal{U}}$ in Fig. 16(c) can be constructed with two controlled-NOT gates [79].

2. Derivation of Eq. (A1)

Here, we shall summarize the derivation of Eq. (A1) following Ref. [53]. Let us first introduce the magic basis $\{|\phi_0\rangle, |\phi_1\rangle, |\phi_2\rangle, |\phi_3\rangle\}$ defined on the two-qubit system $\mathbb{I} = \{i, j\}$:

$$|\phi_0\rangle = \frac{1}{\sqrt{2}}(|00\rangle + |11\rangle),$$
 (A13)

$$|\phi_1\rangle = -\frac{\mathrm{i}}{\sqrt{2}}(|00\rangle - |11\rangle),$$
 (A14)

$$|\phi_2\rangle = \frac{1}{\sqrt{2}}(|01\rangle - |10\rangle),\tag{A15}$$

$$|\phi_3\rangle = -\frac{\mathrm{i}}{\sqrt{2}}(|01\rangle + |10\rangle),$$
 (A16)

where $|00\rangle = |0\rangle_i \otimes |0\rangle_j$, $|11\rangle = |1\rangle_i \otimes |1\rangle_j$, $|01\rangle = |0\rangle_i \otimes |1\rangle_j$, and $|10\rangle = |1\rangle_i \otimes |0\rangle_j$. The unitary transformation $\hat{\mathcal{M}}$ from the magic basis $\{|\phi_0\rangle, |\phi_1\rangle, |\phi_2\rangle, |\phi_3\rangle\}$ to the computational basis $\{|0\rangle, |1\rangle, |2\rangle, |3\rangle\} = \{|00\rangle, |10\rangle, |01\rangle, |11\rangle\}$ is given by

$$\hat{\mathcal{M}} = \sum_{n=0}^{3} \sum_{k=0}^{3} |n\rangle [\boldsymbol{M}]_{nk} \langle \phi_k|, \tag{A17}$$

where $[M]_{nk} = \langle n | \phi_k \rangle$, i.e.,

$$\mathbf{M} = \frac{1}{\sqrt{2}} \begin{pmatrix} 1 & -\mathbf{i} & 0 & 0\\ 0 & 0 & -1 & -\mathbf{i}\\ 0 & 0 & 1 & -\mathbf{i}\\ 1 & \mathbf{i} & 0 & 0 \end{pmatrix}. \tag{A18}$$

Any state $|\psi\rangle$ on the two-qubit system \mathbb{I} can be represented by $|\psi\rangle = \sum_{k=0}^{3} \mu_k |\phi_k\rangle$, where μ_k is generally complex.

Now let $\{|\psi_k\rangle\}_{k=0}^3$ be a basis where $\langle \psi_k | \psi_{k'} \rangle = \delta_{kk'}$ and $|\psi_k\rangle$ are all maximally entangled. We refer to such a basis $\{|\psi_k\rangle\}_{k=0}^3$ as a maximally entangled basis. This representation has several interesting properties. Here, we list only the essential ones to construct the quantum circuit representation of any unitary operator acting on two qubits.

- (i) If $|\psi\rangle$ is real in the magic basis ($\mu_k \in \mathbb{R}$), then $|\psi\rangle$ is maximally entangled. If $|\psi\rangle$ is maximally entangled, then one can choose $|\psi\rangle$ real in the magic basis except for the global phase factor.
- (ii) $\sum_{k=0}^3 \mu_k^2 = 0$ for $|\psi\rangle = \sum_{k=0}^3 \mu_k |\phi_k\rangle$ if and only if $|\psi\rangle$ is a product state.
- (iii) Let $\{|\psi_k\rangle\}_{k=0}^3$ be a maximally entangled basis. Then, one can obtain local unitary operators $\hat{\mathcal{R}}_i$ and $\hat{\mathcal{R}}_j$ and a phase ξ_k such that

$$\hat{\mathcal{R}}_i \hat{\mathcal{R}}_j e^{i\xi_k} |\psi_k\rangle = |\phi_k\rangle. \tag{A19}$$

(iv) For any unitary operator $\hat{\mathcal{U}}$ acting on two qubits, there exist a phase ε_k and two maximally entangled bases $\{|\psi_k\rangle\}_{k=0}^3$ and $\{|\psi_k'\rangle\}_{k=0}^3$ such that

$$\hat{\mathcal{U}}|\psi_k\rangle = e^{\mathrm{i}\varepsilon_k}|\psi_k'\rangle. \tag{A20}$$

(v) The magic states $|\phi_k\rangle$ are the eigenstates of the operator

$$\hat{\mathcal{D}} = e^{-i(\alpha_x \hat{X}_i \hat{X}_j + \alpha_y \hat{Y}_i \hat{Y}_j + \alpha_z \hat{Z}_i \hat{Z}_j)}, \tag{A21}$$

namely, $\hat{\mathcal{D}}|\phi_k\rangle=e^{-\mathrm{i}\lambda_k}|\phi_k\rangle$ with λ_k being given as

$$\lambda_0 = \alpha_x - \alpha_y + \alpha_z + 2\pi n_0, \tag{A22}$$

$$\lambda_1 = -\alpha_x + \alpha_y + \alpha_z + 2\pi n_1, \tag{A23}$$

$$\lambda_2 = -\alpha_x - \alpha_y - \alpha_z + 2\pi n_2, \tag{A24}$$

$$\lambda_3 = \alpha_x + \alpha_y - \alpha_z + 2\pi n_3, \tag{A25}$$

where n_k (k=0,1,2,3) are integers. The proof of the above properties (i)–(v) is outlined in Ref. [53]. Here, we briefly comment on how to find $\hat{\mathcal{R}}_i$, $\hat{\mathcal{R}}_j$, and $e^{\mathrm{i}\xi_k}$ in property (iii), and $\{|\psi_k\rangle\}_{k=0}^3$, $\{|\psi_k'\rangle\}_{k=0}^3$, and $e^{\mathrm{i}\varepsilon_k}$ in property (iv).

In property (iii), one can always choose $|\psi_k\rangle=e^{i\eta_k}|\bar{\psi}_k\rangle$, where $|\bar{\psi}_k\rangle$ is a real in the magic basis [property (i)]. If we define $|\mu\rangle=(|\bar{\psi}_0\rangle+\mathrm{i}|\bar{\psi}_1\rangle)/\sqrt{2}$ and $|\nu\rangle=(|\bar{\psi}_0\rangle-\mathrm{i}|\bar{\psi}_1\rangle)/\sqrt{2}$, then $|\mu\rangle$ and $|\nu\rangle$ are product states such that $|\mu\rangle=|a\rangle_i|b\rangle_j\equiv|ab\rangle$ and $|\nu\rangle=|\bar{a}\rangle_i|\bar{b}\rangle_j\equiv|\bar{a}\bar{b}\rangle$ [80]. Since $|\bar{\psi}_0\rangle$ and $|\bar{\psi}_1\rangle$ are maximally entangled states and $\langle\mu|\nu\rangle=0$, $|a\rangle_i$ and $|\bar{a}\rangle_i$ ($|b\rangle_j$ and $|\bar{b}\rangle_j$) are orthogonal to each other. Similarly, the remaining states $|\bar{\psi}_2\rangle$ and $|\bar{\psi}_3\rangle$ are represented by using the linear combination of $|a\rangle_i|\bar{b}\rangle_j\equiv|a\bar{b}\rangle$ and $|\bar{a}\rangle_i|b\rangle_j\equiv|\bar{a}b\rangle$. Without loss of generality, one can find that $|\bar{\psi}_2\rangle=(e^{\mathrm{i}\delta}|a\bar{b}\rangle-e^{-\mathrm{i}\delta}|\bar{a}b\rangle)/\sqrt{2}$ and thereby $|\bar{\psi}_3\rangle=-\mathrm{i}(e^{\mathrm{i}\delta}|a\bar{b}\rangle+e^{-\mathrm{i}\delta}|\bar{a}b\rangle)/\sqrt{2}$. In this case, if we define

$$\hat{\mathcal{R}}_i = (|0\rangle_i)(_i\langle a|) + (|1\rangle_i)(_i\langle \bar{a}|)e^{i\delta}, \tag{A26}$$

$$\hat{\mathcal{R}}_{i} = (|0\rangle_{i})(_{i}\langle b|) + (|1\rangle_{i})(_{i}\langle \bar{b}|)e^{-i\delta}, \tag{A27}$$

then we can obtain the relation in Eq. (A19) by choosing appropriately the phase factor ξ_k , i.e., $\xi_k = -\eta_k$. In this way, we can obtain the local unitary operators $\hat{\mathcal{R}}_i$ and $\hat{\mathcal{R}}_j$, and the phase factors ξ_k in property (iii).

In property (iv), for a given unitary operator $\hat{\mathcal{U}}$, let $|\psi_k\rangle$ be the eigenstates of the operator $\hat{\mathcal{W}}=\hat{\mathcal{U}}^t\hat{\mathcal{U}}$ with the corresponding eigenvalues $e^{2\mathrm{i}\varepsilon_k}$, where $\hat{\mathcal{U}}^t$ is the transpose of $\hat{\mathcal{U}}$. From the fact that $\hat{\mathcal{W}}^\dagger\hat{\mathcal{W}}=\hat{\mathbb{I}}$ and $\hat{\mathcal{W}}^t=\hat{\mathcal{W}}$, the eigenstates $|\psi_k\rangle$ can be chosen as real in the magic basis and hence $\{|\psi_k\rangle\}_{k=0}^3$ is a maximally entangled basis. From the eigenvalue equation $(\hat{\mathcal{W}}-e^{2\mathrm{i}\varepsilon_k})|\psi_k\rangle=0$, one can readily show that $|\psi_k'\rangle\equiv e^{-\mathrm{i}\varepsilon_k}\hat{\mathcal{U}}|\psi_k\rangle$ is real in the magic basis, suggesting that $\{|\psi_{k'}\rangle\}_{k=0}^3$ is also a maximally entangled basis. Therefore, we obtain the maximally entangled bases $\{|\psi_k\rangle\}_{k=0}^3$ and $\{|\psi_k'\rangle\}_{k=0}^3$, and the phase factor ε_k in property (iv)

Now, let $|\psi_k\rangle$ and $|\psi_k'\rangle$ be the states that satisfy property (iv) for a unitary operator $\hat{\mathcal{U}}$. From property (iii), one can find the set of the local operators $\hat{\mathcal{R}}_i$ and $\hat{\mathcal{R}}_j$ and the phase ξ_k for $|\psi_k\rangle$ such that

$$|\psi_k\rangle = e^{-i\xi_k} \hat{\mathcal{R}}_i^{\dagger} \hat{\mathcal{R}}_i^{\dagger} |\phi_k\rangle. \tag{A28}$$

Similarly, we can also find $\hat{\mathcal{R}}'_i$, $\hat{\mathcal{R}}'_i$, and ξ'_k for $|\psi'_k\rangle$ such that

$$|\psi_i'\rangle = e^{-i\xi_k'} \hat{\mathcal{R}}_i' \hat{\mathcal{R}}_i' |\phi_k\rangle. \tag{A29}$$

Inserting Eqs. (A28) and (A29) into Eq. (A20), we obtain that

$$\hat{\mathcal{U}}e^{-i\xi_k}\hat{\mathcal{R}}_i^{\dagger}\hat{\mathcal{R}}_i^{\dagger}|\phi_k\rangle = e^{i\varepsilon_k}e^{-i\xi_k'}\hat{\mathcal{R}}_i'\hat{\mathcal{R}}_i'|\phi_k\rangle. \tag{A30}$$

Multiplying $(\hat{\mathcal{R}}_i'\hat{\mathcal{R}}_i')^{\dagger}$ from the left, we obtain that

$$(\hat{\mathcal{R}}_{i}^{\prime})^{\dagger}(\hat{\mathcal{R}}_{i}^{\prime})^{\dagger}\hat{\mathcal{U}}\hat{\mathcal{R}}_{i}^{\dagger}\hat{\mathcal{R}}_{i}^{\dagger}|\phi_{k}\rangle = e^{-\mathrm{i}(\xi_{k}^{\prime} - \xi_{k} - \varepsilon_{k})}|\phi_{k}\rangle. \tag{A31}$$

Equation (A31) suggests that the operator $(\hat{\mathcal{R}}_i')^{\dagger}(\hat{\mathcal{R}}_j')^{\dagger}\hat{\mathcal{U}}\hat{\mathcal{R}}_i^{\dagger}\hat{\mathcal{R}}_j^{\dagger}$ becomes identical to $e^{-i\alpha_0}\hat{\mathcal{D}}$ if we choose

$$\alpha_0 + \lambda_k = \xi_k' - \xi_k - \varepsilon_k + 2\pi n_k \tag{A32}$$

for k = 0, 1, 2, 3. Inserting Eqs. (A22)–(A25) into Eq. (A32), we can determine the phase factors α_{μ} ($\mu = 0, x, y, z$) and therefore obtain the following form of the unitary operator $\hat{\mathcal{U}}$:

$$\hat{\mathcal{U}} = e^{-i\alpha_0} \hat{\mathcal{R}}_i' \hat{\mathcal{R}}_i' \hat{\mathcal{D}} \hat{\mathcal{R}}_i \hat{\mathcal{R}}_j. \tag{A33}$$

Since $\hat{\mathcal{R}}_i'$, $\hat{\mathcal{R}}_j'$, $\hat{\mathcal{R}}_i$, and $\hat{\mathcal{R}}_j$ are the single-qubit unitary operators, they can always be represented by the Euler rotations, as described in Appendix B. The two-qubit unitary operator $\hat{\mathcal{D}}$ is represented by the elementary single- and two-qubit gates [77,78], as given in Eq. (A5) and also in Fig. 16(b).

Finally, we note the practical procedure to determine the quantum gates explicitly for a given unitary operator $\hat{\mathcal{U}}$. To assign quantum gates properly for a unitary operator $\hat{\mathcal{U}}$, one has to select an appropriate set of integers n_k for k=0,1,2,3 in Eq. (A32). In addition, there might also be additional phases when the single-qubit unitary operators are represented by the standard single-qubit rotation gates (see Appendix B). Since the number of possible combinations is limited, one can always find the appropriate set of integers n_k by checking all combinations, in practice.

APPENDIX B: PHASE FACTORS IN A SINGLE-QUBIT UNITARY OPERATOR

As shown in Eqs. (A1) and (A33), a two-qubit unitary operator $\hat{\mathcal{U}}$ is generally decomposed into $\hat{\mathcal{U}} = e^{-i\alpha_0} \hat{\mathcal{R}}_i' \hat{\mathcal{R}}_j' \hat{\mathcal{D}} \hat{\mathcal{R}}_i \hat{\mathcal{R}}_j$, where $\hat{\mathcal{R}}_i'$, $\hat{\mathcal{R}}_j'$, $\hat{\mathcal{R}}_i$, and $\hat{\mathcal{R}}_j$ are single-qubit unitary operators. It is well known that these single-qubit operators can be assigned by using the Euler rotation operator given as

$$\hat{\mathcal{R}}(\theta_1, \theta_2, \theta_3) = e^{-i\theta_3 \hat{\mathcal{Z}}/2} e^{-i\theta_2 \hat{Y}/2} e^{-i\theta_1 \hat{\mathcal{Z}}/2}, \tag{B1}$$

where \hat{Y} and \hat{Z} are the Pauli operators acting on the target qubit i or j. However, this is true only when we introduce the overall phase factor θ_0 , as explicitly shown below.

Let us now denote $\hat{V} \in \{\hat{\mathcal{R}}_i', \hat{\mathcal{R}}_j', \hat{\mathcal{R}}_i, \hat{\mathcal{R}}_j\}$ and assume that $\hat{\mathcal{V}}$ is given in the computational basis as

$$\hat{\mathcal{V}} = \sum_{\sigma=0,1} \sum_{\sigma'=0,1} |\sigma\rangle [V]_{\sigma\sigma'} \langle \sigma'|, \tag{B2}$$

where V is the matrix representation of $\hat{\mathcal{V}}$ with the element $[V]_{\sigma\sigma'} = v_{\sigma\sigma'}$. The single-qubit operator $\hat{\mathcal{V}}$ can be assigned by using the Euler rotation operator as

$$\hat{\mathcal{V}} = e^{-i\theta_0/2} \hat{\mathcal{R}}(\theta_1, \theta_2, \theta_3). \tag{B3}$$

Here, the matrix representation \mathbf{R} of $\hat{\mathcal{R}}(\theta_1, \theta_2, \theta_3)$ in the computational basis is given by

$$\mathbf{R} = \begin{pmatrix} e^{-i(\theta_3 + \theta_1)/2} \cos(\theta_2/2) & -e^{-i(\theta_3 - \theta_1)/2} \sin(\theta_2/2) \\ e^{i(\theta_3 - \theta_1)/2} \sin(\theta_2/2) & e^{i(\theta_3 + \theta_1)/2} \cos(\theta_2/2) \end{pmatrix}.$$
(B4)

Therefore, one can deterime θ_0 , θ_1 , θ_2 , and θ_3 by solving the following simultaneous nonlinear equations:

$$v_{00} = e^{-i(\theta_0 + \theta_3 + \theta_1)/2} \cos(\theta_2/2),$$
 (B5)

$$v_{10} = e^{-i(\theta_0 - \theta_3 + \theta_1)/2} \sin(\theta_2/2),$$
 (B6)

$$v_{01} = -e^{-i(\theta_0 + \theta_3 - \theta_1)/2} \sin(\theta_2/2),$$
 (B7)

$$v_{11} = e^{-i(\theta_0 - \theta_3 - \theta_1)/2} \cos(\theta_2/2).$$
 (B8)

We can readily find that the solution of these equations is given as

$$\theta_0 = i \ln \left(v_{00} v_{11} - v_{10} v_{01} \right) + 2\pi m_0, \tag{B9}$$

$$\theta_1 = \frac{i}{2} \ln \left(-\frac{v_{00}v_{10}}{v_{11}v_{01}} \right) + \pi m_1, \tag{B10}$$

$$\theta_2 = \pm \arccos \frac{v_{00}v_{11} + v_{10}v_{01}}{v_{00}v_{11} - v_{10}v_{01}} + 2\pi m_2, \tag{B11}$$

$$\theta_3 = \frac{i}{2} \ln \left(-\frac{v_{00}v_{01}}{v_{11}v_{10}} \right) + \pi m_3 \tag{B12}$$

for $v_{01}v_{10} \neq 0$ and $v_{00}v_{11} \neq 0$. Here, m_i (i = 0, 1, 2, 3) is an integer number that is determined to reproduce the sign of the original matrix elements $v_{\sigma\sigma'}$.

For $v_{01} = v_{10} = 0$ but $v_{00}v_{11} \neq 0$, we can set $\theta_2 = 0$ and thus the Euler rotation is simply the rotation around the z axis. Therefore, only $\theta_1 + \theta_3$ is relevant and we set $\theta_3 = 0$ without losing generality. The solution is thus given as

$$\theta_0 = i \ln (v_{00}v_{11}) + 2\pi m_0,$$
 (B13)

$$\theta_1 = i \ln \left(\frac{v_{00}}{v_{11}} \right) + 2\pi m_1,$$
(B14)

$$\theta_2 = 0, \tag{B15}$$

$$\theta_3 = 0. \tag{B16}$$

For $v_{00}=v_{11}=0$ but $v_{01}v_{10}\neq 0$, we can set $\theta_2=\pi$ without losing generality. Similar to the previous case, we can also set $\theta_3=0$ because $e^{-\mathrm{i}\pi\hat{Y}/2}=-\mathrm{i}\hat{Y}$ and thus $\theta_3-\theta_1$ is relevant. The solution is therefore given as

$$\theta_0 = i \ln (-v_{10}v_{01}) + 2\pi m_0,$$
 (B17)

$$\theta_1 = i \ln \left(-\frac{v_{10}}{v_{01}} \right) + 2\pi m_1,$$
(B18)

$$\theta_2 = \pi, \tag{B19}$$

$$\theta_3 = 0. \tag{B20}$$

APPENDIX C: ADDITIONAL INFORMATION FOR THE EXPERIMENTAL DEMONSTRATION

Here, we provide the coefficients $\psi^r_{\sigma_0\sigma_1}$ and $\psi^r_{\sigma_0\sigma_1\sigma_2}$ in the ramdom states $|\Psi_{2QR}\rangle$ and $|\Psi_{3QR}\rangle$, respectively, as defined in Eqs. (65) and (71). These random states are used for the experimental demonstration in Sec. IV. The method to generate the random states is described in Sec. IV A.

The random state $|\Psi_{2QR}\rangle$ in the two-qubit space used for the experimental demonstration is given by

$$\begin{split} |\Psi_{2QR}\rangle &= (0.36179353 + i0.42519915)|00\rangle \\ &+ (0.14876111 + i0.33156910)|10\rangle \\ &+ (-0.02356009 + i0.68066637)|01\rangle \\ &+ (0.23101109 - i0.19752287)|11\rangle. \end{split}$$
 (C1)

The random state $|\Psi_{3QR}\rangle$ in the three-qubit space used for the experimental demonstration is given by

$$\begin{split} |\Psi_{3QR}\rangle &= (-0.41507377 + i0.14526187)|000\rangle \\ &+ (0.03169105 + i0.35848024)|100\rangle \\ &+ (-0.23166622 + i0.21332733)|010\rangle \\ &+ (-0.32248929 - i0.06104028)|110\rangle \\ &+ (-0.11551530 + i0.13972069)|001\rangle \\ &+ (0.26960898 - i0.03973709)|101\rangle \\ &+ (0.00215509 + i0.44364270)|011\rangle \\ &+ (0.01417350 + i0.40747913)|111\rangle. \end{split}$$

- [1] M. Cerezo, A. Arrasmith, R. Babbush, S. C. Benjamin, S. Endo, K. Fujii, J. R. McClean, K. Mitarai, X. Yuan, L. Cincio, and P. J. Coles, Variational quantum algorithms, Nat. Rev. Phys. 3, 625 (2021).
- [2] A. Peruzzo, J. McClean, P. Shadbolt, M.-H. Yung, X.-Q. Zhou, P. J. Love, A. Aspuru-Guzik, and J. L. O'Brien, A variational eigenvalue solver on a photonic quantum processor, Nat. Commun. 5, 4213 (2014).
- [3] M.-H. Yung, J. Casanova, A. Mezzacapo, J. McClean, L. Lamata, A. Aspuru-Guzik, and E. Solano, From transistor to trapped-ion computers for quantum chemistry, Sci. Rep. 4, 3589 (2014).
- [4] P. J. J. O'Malley, R. Babbush, I. D. Kivlichan, J. Romero, J. R. McClean, R. Barends, J. Kelly, P. Roushan, A. Tranter, N. Ding, B. Campbell, Y. Chen, Z. Chen, B. Chiaro, A. Dunsworth, A. G. Fowler, E. Jeffrey, E. Lucero, A. Megrant, J. Y. Mutus *et al.*, Scalable quantum simulation of molecular energies, Phys. Rev. X 6, 031007 (2016).
- [5] A. Kandala, A. Mezzacapo, K. Temme, M. Takita, M. Brink, J. M. Chow, and J. M. Gambetta, Hardware-efficient variational quantum eigensolver for small molecules and quantum magnets, Nature (London) 549, 242 (2017).
- [6] Y. Shen, X. Zhang, S. Zhang, J.-N. Zhang, M.-H. Yung, and K. Kim, Quantum implementation of the unitary coupled cluster

- for simulating molecular electronic structure, Phys. Rev. A **95**, 020501(R) (2017).
- [7] J. Romero, R. Babbush, J. R. McClean, C. Hempel, P. J. Love, and A. Aspuru-Guzik, Strategies for quantum computing molecular energies using the unitary coupled cluster ansatz, Quantum Sci. Technol. 4, 014008 (2018).
- [8] F. A. Evangelista, G. K.-L. Chan, and G. E. Scuseria, Exact parameterization of fermionic wave functions via unitary coupled cluster theory, J. Chem. Phys. 151, 244112 (2019).
- [9] S. McArdle, S. Endo, A. Aspuru-Guzik, S. C. Benjamin, and X. Yuan, Quantum computational chemistry, Rev. Mod. Phys. 92, 015003 (2020).
- [10] P. Rebentrost, M. Mohseni, and S. Lloyd, Quantum support vector machine for big data classification, Phys. Rev. Lett. 113, 130503 (2014).
- [11] M. Schuld, I. Sinayskiy, and F. Petruccione, An introduction to quantum machine learning, Contemp. Phys. **56**, 172 (2015).
- [12] P. Wittek, *Quantum Machine Learning: What Quantum Computing Means to Data Mining*, 1st ed. (Elsevier, San Diego, CA, 2014).
- [13] J. Adcock, E. Allen, M. Day, S. Frick, J. Hinchliff, M. Johnson, S. Morley-Short, S. Pallister, A. Price, and S. Stanisic, Advances in quantum machine learning, arXiv:1512.02900.
- [14] J. Biamonte, P. Wittek, N. Pancotti, P. Rebentrost, N. Wiebe, and S. Lloyd, Quantum machine learning, Nature (London) 549, 195 (2017).
- [15] M. Schuld and F. Petruccione, Supervised Learning with Quantum Computers, 1st ed. (Springer, Berlin, 2018).
- [16] A. Perdomo-Ortiz, M. Benedetti, J. Realpe-Gómez, and R. Biswas, Opportunities and challenges for quantum-assisted machine learning in near-term quantum computers, Quantum Sci. Technol. 3, 030502 (2018).
- [17] K. Mitarai, M. Negoro, M. Kitagawa, and K. Fujii, Quantum circuit learning, Phys. Rev. A 98, 032309 (2018).
- [18] M. Schuld and N. Killoran, Quantum machine learning in feature hilbert spaces, Phys. Rev. Lett. 122, 040504 (2019).
- [19] V. Havlíček, A. D. Córcoles, K. Temme, A. W. Harrow, A. Kandala, J. M. Chow, and J. M. Gambetta, Supervised learning with quantum-enhanced feature spaces, Nature (London) 567, 209 (2019).
- [20] S.-I. Amari, Natural gradient works efficiently in learning, Neural Comput. 10, 251 (1998).
- [21] K. Seki, T. Shirakawa, and S. Yunoki, Symmetry-adapted variational quantum eigensolver, Phys. Rev. A **101**, 052340 (2020).
- [22] J. Stokes, J. Izaac, N. Killoran, and G. Carleo, Quantum natural gradient, Quantum 4, 269 (2020).
- [23] K. M. Nakanishi, K. Fujii, and S. Todo, Sequential minimal optimization for quantum-classical hybrid algorithms, Phys. Rev. Res. 2, 043158 (2020).
- [24] J. R. McClean, S. Boixo, V. N. Smelyanskiy, R. Babbush, and H. Neven, Barren plateaus in quantum neural network training landscapes, Nat. Commun. 9, 4812 (2018).
- [25] M. Cerezo, A. Sone, T. Volkoff, L. Cincio, and P. J. Coles, Cost function dependent barren plateaus in shallow parametrized quantum circuits, Nat. Commun. 12, 1791 (2021).
- [26] S. Wang, E. Fontana, M. Cerezo, K. Sharma, A. Sone, L. Cincio, and P. J. Coles, Noise-induced barren plateaus in variational quantum algorithms, Nat. Commun. 12, 6961 (2021).

- [27] C. Ortiz Marrero, M. Kieferová, and N. Wiebe, Entanglementinduced barren plateaus, PRX Quantum 2, 040316 (2021).
- [28] C. Dankert, R. Cleve, J. Emerson, and E. Livine, Exact and approximate unitary 2-designs and their application to fidelity estimation, Phys. Rev. A **80**, 012304 (2009).
- [29] S. Sim, P. D. Johnson, and A. Aspuru-Guzik, Expressibility and entangling capability of parameterized quantum circuits for hybrid quantum-classical algorithms, Adv. Quantum Technol. 2, 1900070 (2019).
- [30] T. Hubregtsen, J. Pichlmeier, P. Stecher, and K. Bertels, Evaluation of parameterized quantum circuits: On the relation between classification accuracy, expressibility, and entangling capability, Quantum Mach. Intell. 3, 9 (2021).
- [31] A. W. Harrow and R. A. Low, Random quantum circuits are approximate 2-designs, Commun. Math. Phys. 291, 257 (2009).
- [32] I. T. Diniz and D. Jonathan, Comment on "Random quantum circuits are approximate 2-designs" by A. W. Harrow and R. A. Low [Commun. Math. Phys. 291, 257 (2009)], Commun. Math. Phys. 304, 281 (2011).
- [33] Z. Holmes, K. Sharma, M. Cerezo, and P. J. Coles, Connecting ansatz expressibility to gradient magnitudes and barren plateaus, PRX Quantum 3, 010313 (2022).
- [34] T. Haug, K. Bharti, and M. S. Kim, Capacity and quantum geometry of parametrized quantum circuits, PRX Quantum 2, 040309 (2021).
- [35] K. Mitarai, Y. Suzuki, W. Mizukami, Y. O. Nakagawa, and K. Fujii, Quadratic clifford expansion for efficient benchmarking and initialization of variational quantum algorithms, Phys. Rev. Res. 4, 033012 (2022).
- [36] G. Vidal, Entanglement renormalization, Phys. Rev. Lett. 99, 220405 (2007).
- [37] G. Vidal, Class of quantum many-body states that can be efficiently simulated, Phys. Rev. Lett. 101, 110501 (2008).
- [38] G. Evenbly and G. Vidal, Algorithms for entanglement renormalization, Phys. Rev. B **79**, 144108 (2009).
- [39] I. Cong, S. Choi, and M. D. Lukin, Quantum convolutional neural networks, Nat. Phys. 15, 1273 (2019).
- [40] A. Pesah, M. Cerezo, S. Wang, T. Volkoff, A. T. Sornborger, and P. J. Coles, Absence of barren plateaus in quantum convolutional neural networks, Phys. Rev. X 11, 041011 (2021).
- [41] H. R. Grimsley, S. E. Economou, E. Barnes, and N. J. Mayhall, An adaptive variational algorithm for exact molecular simulations on a quantum computer, Nat. Commun. 10, 3007 (2019).
- [42] H. L. Tang, V. O. Shkolnikov, G. S. Barron, H. R. Grimsley, N. J. Mayhall, E. Barnes, and S. E. Economou, Qubit-adaptvqe: An adaptive algorithm for constructing hardware-efficient ansätze on a quantum processor, PRX Quantum 2, 020310 (2021).
- [43] J. Liu, Z. Li, and J. Yang, An efficient adaptive variational quantum solver of the Schrödinger equation based on reduced density matrices, J. Chem. Phys. **154**, 244112 (2021).
- [44] Y.-X. Yao, N. Gomes, F. Zhang, C.-Z. Wang, K.-M. Ho, T. Iadecola, and P. P. Orth, Adaptive variational quantum dynamics simulations, PRX Quantum **2**, 030307 (2021).
- [45] F. Zhang, N. Gomes, Y. Yao, P. P. Orth, and T. Iadecola, Adaptive variational quantum eigensolvers for highly excited states, Phys. Rev. B **104**, 075159 (2021).
- [46] H. F. Trotter, On the product of semi-groups of operators, Proc. Amer. Math. Soc. 10, 545 (1959).

- [47] M. Suzuki, Relationship between d-dimensional quantal spin systems and (d+1)-dimensional Ising systems: Equivalence, critical exponents and systematic approximants of the partition function and spin correlations, Prog. Theor. Phys. **56**, 1454 (1976).
- [48] S. Lloyd, Universal quantum simulators, Science 273, 1073 (1996).
- [49] IBM, Ibm quantum, https://quantum-computing.ibm.com.
- [50] M. Cerezo, K. Sharma, A. Arrasmith, and P. J. Coles, Variational quantum state eigensolver, npj Quantum Inf. 8, 113 (2022).
- [51] Apart from a global phase factor that is irrelevant to the discussion here.
- [52] M. A. Nielsen and I. L. Chuang, Quantum Computation and Quantum Information: 10th Anniversary Edition (Cambridge University Press, New York, NY, 2011).
- [53] B. Kraus and J. I. Cirac, Optimal creation of entanglement using a two-qubit gate, Phys. Rev. A 63, 062309 (2001).
- [54] V. Bergholm, J. J. Vartiainen, M. Möttönen, and M. M. Salomaa, Quantum circuits with uniformly controlled one-qubit gates, Phys. Rev. A 71, 052330 (2005).
- [55] M. Schuld and F. Petruccione, Supervised Learning with Quantum Computers (Springer, Cham, 2019).
- [56] H.-Q. Zhou, R. Orús, and G. Vidal, Ground state fidelity from tensor network representations, Phys. Rev. Lett. 100, 080601 (2008).
- [57] T. Shirakawa, K. Seki, and S. Yunoki, Discretized quantum adiabatic process for free fermions and comparison with the imaginary-time evolution, Phys. Rev. Res. 3, 013004 (2021).
- [58] R. Barends, L. Lamata, J. Kelly, L. García-Álvarez, A. G. Fowler, A. Megrant, E. Jeffrey, T. C. White, D. Sank, J. Y. Mutus, B. Campbell, Y. Chen, Z. Chen, B. Chiaro, A. Dunsworth, I.-C. Hoi, C. Neill, P. J. J. O'Malley, C. Quintana, P. Roushan *et al.*, Digital quantum simulation of fermionic models with a superconducting circuit, Nat. Commun. 6, 7654 (2015).
- [59] R. Barends, A. Shabani, L. Lamata, J. Kelly, A. Mezzacapo, U. L. Heras, R. Babbush, A. G. Fowler, B. Campbell, Y. Chen, Z. Chen, B. Chiaro, A. Dunsworth, E. Jeffrey, E. Lucero, A. Megrant, J. Y. Mutus, M. Neeley, C. Neill, P. J. J. O'Malley et al., Digitized adiabatic quantum computing with a superconducting circuit, Nature (London) 534, 222 (2016).
- [60] R. Haghshenas, J. Gray, A. C. Potter, and G. K.-L. Chan, Variational power of quantum circuit tensor networks, Phys. Rev. X 12, 011047 (2022).
- [61] S. Anand, J. Hauschild, Y. Zhang, A. C. Potter, and M. P. Zaletel, Holographic quantum simulation of entanglement renormalization circuits, PRX Quantum 4, 030334 (2023).
- [62] G. Evenbly and G. Vidal, Tensor network states and geometry, J. Stat. Phys. 145, 891 (2011).
- [63] H.-K. Zhang, S. Liu, and S.-X. Zhang, Absence of barren plateaus in finite local-depth circuits with long-range entanglement, Phys. Rev. Lett. 132, 150603 (2024).

- [64] M. Schuld, I. Sinayskiy, and F. Petruccione, Prediction by linear regression on a quantum computer, Phys. Rev. A 94, 022342 (2016).
- [65] L. K. Grover, Synthesis of quantum superpositions by quantum computation, Phys. Rev. Lett. 85, 1334 (2000).
- [66] V. V. Shende, S. S. Bullock, and I. L. Markov, Synthesis of quantum-logic circuits, IEEE Trans. Comput. Aided Des. Integr. Circuits Syst. 25, 1000 (2006).
- [67] M. Plesch and Časlav Brukner, Quantum-state preparation with universal gate decompositions, Phys. Rev. A 83, 032302 (2011).
- [68] Y. R. Sanders, G. H. Low, A. Scherer, and D. W. Berry, Black-box quantum state preparation without arithmetic, Phys. Rev. Lett. 122, 020502 (2019).
- [69] S.-J. Ran, Encoding of matrix product states into quantum circuits of one- and two-qubit gates, Phys. Rev. A 101, 032310 (2020).
- [70] P.-F. Zhou, R. Hong, and S.-J. Ran, Automatically differentiable quantum circuit for many-qubit state preparation, Phys. Rev. A 104, 042601 (2021).
- [71] K. Nakaji, S. Uno, Y. Suzuki, R. Raymond, T. Onodera, T. Tanaka, H. Tezuka, N. Mitsuda, and N. Yamamoto, Approximate amplitude encoding in shallow parameterized quantum circuits and its application to financial market indicators, Phys. Rev. Res. 4, 023136 (2022).
- [72] Standard test images available at ImageProcessingPlace.com.
- [73] E. Stoudenmire and D. J. Schwab, Supervised learning with tensor networks, in *Advances in Neural Information Processing Systems*, edited by D. Lee, M. Sugiyama, U. Luxburg, I. Guyon, and R. Garnett (Curran Associates, Inc., Red Hook, NY, 2016), Vol. 29.
- [74] L. Placidi, R. Hataya, T. Mori, K. Aoyama, H. Morisaki, K. Mitarai, and K. Fujii, MNISQ: A large-scale quantum circuit dataset for machine learning on/for quantum computers in the NISQ era, arXiv:2306.16627.
- [75] G. Aleksandrowicz, T. Alexander, P. Barkoutsos, L. Bello, Y. Ben-Haim, D. Bucher, F. J. Cabrera-Hernández, J. Carballo-Franquis, A. Chen, C.-F. Chen, J. M. Chow, A. D. Córcoles-Gonzales, A. J. Cross, A. Cross, J. Cruz-Benito, C. Culver, S. De La P. González, E. De L. Torre, D. Ding, E. Dumitrescu et al., Qiskit: An open-source framework for quantum computing, Zenodo, 2019, doi: 10.5281/zenodo.2562111.
- [76] F. Mezzadri, How to generate random matrices from the classical compact groups, arXiv:math-ph/0609050.
- [77] G. Vidal and C. M. Dawson, Universal quantum circuit for two-qubit transformations with three controlled-not gates, Phys. Rev. A 69, 010301(R) (2004).
- [78] M. W. Coffey, R. Deiotte, and T. Semi, Comment on "Universal quantum circuit for two-qubit transformations with three controlled-not gates" and "Recognizing small-circuit structure in two-qubit operators," Phys. Rev. A 77, 066301 (2008).
- [79] F. Vatan and C. Williams, Optimal quantum circuits for general two-qubit gates, Phys. Rev. A 69, 032315 (2004).
- [80] In practice, we can obtain, for example, $|a\rangle_i$ and $|b\rangle_j$ by performing the SVD of the matrix $\mu_{nn'}$, where $\mu_{nn'}$ is defined as $|\mu\rangle = (|\bar{\Psi}_0\rangle + \mathrm{i}|\bar{\Psi}_1\rangle)/\sqrt{2} = \sum_{n=0}^1 \sum_{n'=0}^1 \mu_{nn'} |n\rangle_i |n'\rangle_j$.